Tectono-Magmatic Evolution of Asymmetric Coronae on Venus: Topographic Classification and 3D Thermo-Mechanical Modeling

Author(s):
Gülcher, Anna J.P.; Yu, Ting-Ying; Gerya, Taras V.

Publication date:
2023-11

Permanent link:
https://doi.org/10.3929/ethz-b-000640127

Originally published in:
Journal of Geophysical Research: Planets 128(11), https://doi.org/10.1029/2023JE007978

Funding acknowledgement:
ETH-33 16-1 - The persistence primordial domains in the mantle of Earth and Mars (ETHZ)

JGR Planets

RESEARCH ARTICLE
10.1029/2023JE007978

Key Points:

- A new topographic classification of large coronae on Venus reveals that most coronae are radially asymmetric and bound a topographic margin
- We present 3D tectono-magmatic models of plume-margin interactions on Venus which reveal several geodynamic evolution scenarios
- Lateral lithospheric changes and the basalt-to-eclogite phase change mostly control the tectonic styles and coronae activity lifetime

Supporting Information:

Supporting Information may be found in the online version of this article.

Correspondence to:

A. J. P. Gülcher,
anna.gulcher@caltech.edu

Citation:

Gülcher, A. J. P., Yu, T.-Y., & Gerya, T. V. (2023). Tectono-magmatic evolution of asymmetric coronae on Venus: Topographic classification and 3D thermo-mechanical modeling. *Journal of Geophysical Research: Planets*, *128*, e2023JE007978. https://doi.org/10.1029/2023JE007978

Received 5 JUL 2023
Accepted 3 OCT 2023

Author Contributions:

Conceptualization: Anna J. P. Gülcher, Taras V. Gerya
Investigation: Anna J. P. Gülcher, Ting-Ying Yu
Methodology: Anna J. P. Gülcher
Software: Anna J. P. Gülcher, Taras V. Gerya
Supervision: Anna J. P. Gülcher, Taras V. Gerya
Validation: Anna J. P. Gülcher
Visualization: Anna J. P. Gülcher, Ting-Ying Yu

Tectono-Magmatic Evolution of Asymmetric Coronae on Venus: Topographic Classification and 3D Thermo-Mechanical Modeling

Anna J. P. Gülcher[1,2,3], Ting-Ying Yu[4], and Taras V. Gerya[3]

[1]Seismological Laboratory, Division of Geological and Planetary Sciences, California Institute of Technology, Pasadena, CA, USA, [2]Division of Planetary Interiors and Geophysics, NASA Jet Propulsion Laboratory, Caltech, Pasadena, CA, USA, [3]Department of Earth Sciences, Institute of Geophysics, ETH Zurich, Zurich, Switzerland, [4]Center for Computational Science and Engineering (CCSE), Department of Mechanical Engineering, Massachusetts Institute of Technology, Cambridge, MA, USA

Abstract Venus is the only other Earth-sized planet in the Solar System but it does not exhibit evidence of plate tectonics that dominates geological processes on Earth. Surface deformation on Venus is mainly driven by mantle convection and plume-lithosphere interactions, likely represented by the widespread development of the circular volcano-tectonic features known as coronae. Here, we present a joint study of mission data analysis and 3D modeling of asymmetric coronae on Venus. We systematically analyze 155 of the largest coronae on Venus in terms of surface topography and morphology. We establish that 75% of those coronae are radially asymmetric, and further sub-categorize them based on their adjacent topography. This analysis reveals that many asymmetric coronae are positioned at a topographic transition between a lowland and plateau (termed topographic margin). With state-of-the-art 3D numerical models, we investigate the physical processes behind plume-margin interactions on Venus. We find that several tectonic styles may be responsible for asymmetric coronae at topographic margins, including lowland-sided subduction, plateau-sided lithospheric dripping, and an embedded plume. The gradient in lithospheric strength across the topographic margin controls these tectonic styles, and larger gradients enhance lithospheric resurfacing and the lifetime of the coronae. We also find that the density increase associated with the basalt-to-eclogite phase change provides the extra negative gravitational force required for downgoing crust to be recycled into the mantle. The models presented in this study reproduce a wide set of asymmetrical corona features found on Venus and suggest that they are generally more long-lived than symmetric coronae.

Plain Language Summary Venus surface tectonics and volcanism are very dissimilar to modern Earth and in particular show development of many hundreds of circular and oval-shaped "corona" structures, ranging in size from 60 to nearly 2,000 km. Here, the 155 largest coronae on Venus are systematically analyzed in terms of surface morphology and topographic positioning. We establish that the vast majority of large coronae on Venus have asymmetric features and are positioned at a topographic margin. We present the first-ever plume-margin numerical models in 3D which show several tectonic styles of plume-margin interactions on Venus. The styles depend on the lithospheric structure and the density change of crustal material at depth. Importantly, the models indicate that asymmetric coronae at topographic margins are longer lived structures that symmetric coronae.

1. Introduction

Understanding the dynamic mechanisms responsible for Venus' geological history remains a key objective in terrestrial planetary sciences, as it helps to answer why Earth and Venus have undergone such staggeringly divergent evolutionary paths (O'Rourke et al., 2023). Even though the planets have similar size, mass, and chemical makeup, their surface environments could not be more different. Whereas Earth's environment is habitable, Venus obtains a crushingly thick atmosphere over a hellish surface. Venus' extremely hot surface temperatures (~500°C), its rocky, basalt-like surface, and likely dry interior were revealed in early spacecraft exploration of Venus (e.g., Phillips & Malin, 1983; Surkov et al., 1984). The culmination of Venus science was initiated by the near-global coverage geophysical data set from the Magellan spacecraft (NASA, 1990–1994) (J. P. Ford et al., 1993). The NASA Magellan mission yielded the first "high-resolution" (~100 m/pixel) global synthetic

Writing – original draft: Anna J. P. Gülcher
Writing – review & editing: Taras V. Gerya

aperture radar (SAR) image mosaic of the planet, as well as topographic and emissivity data sets (e.g., Saunders et al., 1990), which showed Venus to be a world with distinguishable lava flows, major rift zones, thousands of shield volcanoes (Hahn & Byrne, 2023; Head et al., 1992), as well as more exotic volcano-tectonic landforms such as the distinctive corona structures (Stofan et al., 1992). Impact craters appear to be randomly distributed and relatively sparse, although there are some significant differences in crater spatial density between different geomorphologic map units or topographic elevations (Herrick et al., 2023). Overall, these observations led to the interpretation of a young Venusian surface age of ∼500–700 Myr (e.g., Strom et al., 1994; Turcotte, 1993). Moreover, it was found that plate tectonics does not seem to operate on Venus at the present-day, raising questions regarding the style of tectonics and geodynamics that shape(d) the planet's geology. With a set new missions to Venus in the pipeline, our current efforts to understand the planet rely on past mission data, such as Magellan, and the usage of ever-improving research technologies.

The apparent young and uniform surface age of Venus and the absence of plate tectonics was initially ascribed as resulting from a global resurfacing event 500–700 Myr ago (Strom et al., 1994; Turcotte, 1993), but more recent studies shed light on ongoing regional resurfacing that can lead to a similar observations (Bjonnes et al., 2012; Herrick & Rumpf, 2011). Moreover, numerous sites of thin elastic lithospheres were found which indicate relatively high heat flow (e.g., Anderson & Smrekar, 2006; Borrelli et al., 2021; O'Rourke & Smrekar, 2018; Smrekar et al., 2010, 2023), and countless examples of indirect evidence have argued for active tectonics and volcanism on Venus on geological timescales (e.g., Campbell et al., 2017; D'Incecco et al., 2017; Esposito, 1984; Filiberto et al., 2020; Gülcher et al., 2020). Recently, Herrick and Hensley (2023) discovered surface changes of a volcanic vent in Magellan mission data during a 8-month time window in 1991, which is perhaps the best argument for present-day volcanic activity on Venus. Surface deformation on Venus is dominated by mantle plumes, magmatic intrusions, lithospheric delamination, and regional resurfacing processes (e.g., Adams et al., 2022; Lourenço et al., 2020; Rolf et al., 2022). The enigmatic corona structures likely play a key role in this global tectonic concept.

Venus' coronae are ∼circular and oval-shaped structures ranging in diameter from 60 km to nearly 2,000 km that are widespread on the surface (Glaze et al., 2002; Stofan et al., 1992, 2001). Over 500 coronae have been identified on Venus and the structures are usually related to surface fracturing, various topographic profiles, and volcanism (e.g., Smrekar & Stofan, 1997). Their origins are contentious but the most common explanation suggests an interaction of the Venus lithosphere with mantle plumes (cf. reviews in Grindrod & Hoogenboom, 2006; Gülcher et al., 2020; Krassilnikov, 2003). Some coronae are inferred to host plate-boundary processes such as subduction at (part of) their arc (e.g., Davaille et al., 2017; McKenzie et al., 1992; Sandwell & Schubert, 1992). Several numerical studies have been carried out investigating coronae formation via plume-lithosphere interactions (Gerya, 2014; Gülcher et al., 2020; Piskorz et al., 2014). Yet, most of these previous studies investigated plume impingement upon a laterally homogeneous lithosphere (Gerya, 2014; Gülcher et al., 2020), and all of the studies only addressed the formation of symmetric coronae structures. In nature, many Venusian coronae show more complex morphologies than those obtained in those studies. This includes coronae with partial or no fractured annuli (Glaze et al., 2002; Stofan et al., 2001), with shapes diverging from being circular, with single-sided trenches and rims, or with strongly tilted topographies. Moreover, although absolute estimates differ, the Venusian surface is laterally heterogeneous in terms of crustal thickness and lithospheric strength (Anderson & Smrekar, 2006; James et al., 2013; Wieczorek, 2015), which likely affects the surface expressions of plume-lithosphere interactions.

2. Analysis of Coronae on Venus

We present our new systematic analysis of the 155 largest coronae on Venus in terms of surface topography and radial (a)symmetry. These coronae have a diameter at least 300 km. We use the coronae database from Gülcher et al. (2020), extended with 20 additional large coronae that meet the diameter requirement from Stofan et al. (1992), and analyze each corona's topography with the Generic Mapping Tools software package (Wessel & Luis, 2017) using the Magellan global topography data (P. G. Ford, 1992). We examine the radial topographic (a)symmetry of each corona, and their relation to their surroundings. We define (a)symmetry based on the topographic features (troughs, rims, rises) displayed and their variability across the coronae, which differs from the (a)symmetry definition from Stofan et al. (1992) based on SAR imagery-only (see below). The full classification database is available on Zenodo (Gülcher, 2023), see Text S1.1 in Supporting Information S1. Out of the

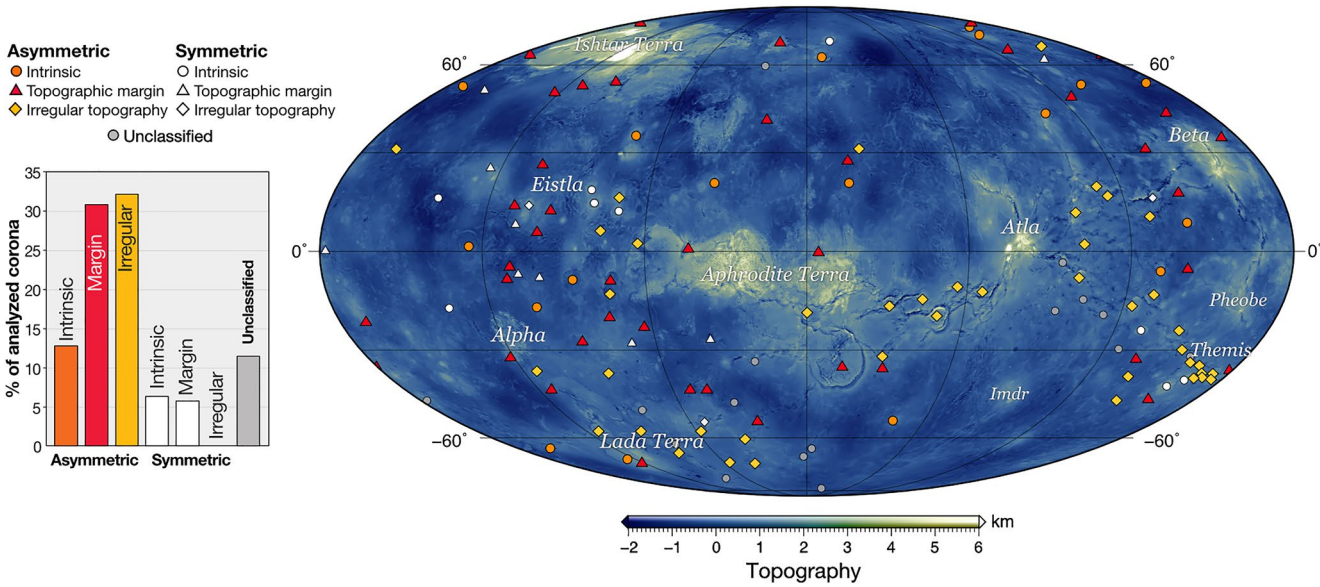

Figure 1. Histogram and global distribution of coronae identified as radially symmetric asymmetric, and the different subcategories identified (see main text). A Mollweide projection centered at 120°E is utilized for the map. Coronae are plotted on the global topography (P. G. Ford, 1992) relative to 6051.877 km. Coronae that were analyzed but could not be classified are additionally shown in Figure S1 in Supporting Information S1, which also includes the surface distribution of rifted regions (Price et al., 1996) and tesserae (Ivanov & Head, 1996) on Venus. A complete record of classifications for all 155 coronae is provided on Zenodo (Gülcher, 2023).

analyzed coronae, only 13% can be considered radially symmetric, meaning that the topographic features of their radial profile are independent of the angle of the cross section through the corona (see Text S1.2 and Figure S2 in Supporting Information S1). We establish that 75% of analyzed coronae display an asymmetric topography profile, meaning that the topographic features displayed (rims, trenches, domes) vary with the angle of cross section through the corona. The remaining coronae (12%) are inconclusive because their topography present ambiguous characteristics which inhibited classification.

For each of the categories defined above, we further define three sub-classes based on their relation to their surrounding topography: intrinsically (a)symmetric (I), topographic margin (II), and irregular topography (III). The map distribution of this survey is given in Figure 1 and Figure S1 in Supporting Information S1. Below, a detailed description of the classification and spatial distribution of asymmetric corona sub-classes is given.

I. Intrinsically asymmetric (17%). A small portion of asymmetric coronae are intrinsically asymmetric. Such coronae are situated in a region of otherwise ~homogeneous topography (with little topography variations, away from any large-scale structures). This positioning suggests that the coronae's asymmetric morphology is intrinsically formed during their development. For example, the Ereshkigal corona displays a partial rise and rim within a region of uniform low topography (Figure 2a). The intrinsically asymmetric coronae are distributed throughout the Venusian surface, often away from chasmatae and topographic highlands (Figure 1).

II. Topographic margin (41%). Many asymmetric coronae are partially bounded by a region of high-topography, that is, a plateau (Figure 1). The regional topography changes from the high plateau to a (relative) lowland within 100s of km. This transition from a topographic lowland to a plateau is hereafter termed as "topographic margin." The features of the radial topographic profile of these coronae often changes across the margin, such as is the case for Ma corona (Figure 2b). These "topographic margin" coronae are one of the most common types of asymmetric coronae. Some, but not necessarily all coronae in this class are partially bounded by tesserae (see Figure S1 in Supporting Information S1).

III. Irregular topography (42%). An asymmetric corona is categorized as "Irregular topography" if it is bounded by a complex topographic terrain, making the individual shape and topographic profile of the corona difficult to recognize in the topography data at hand. Many of these coronae are situated at, or near, chasmata rifts and/or appear as corona clusters (Figure 1). This is the case for for example, the Lilwani coronae (Figure 2c), which

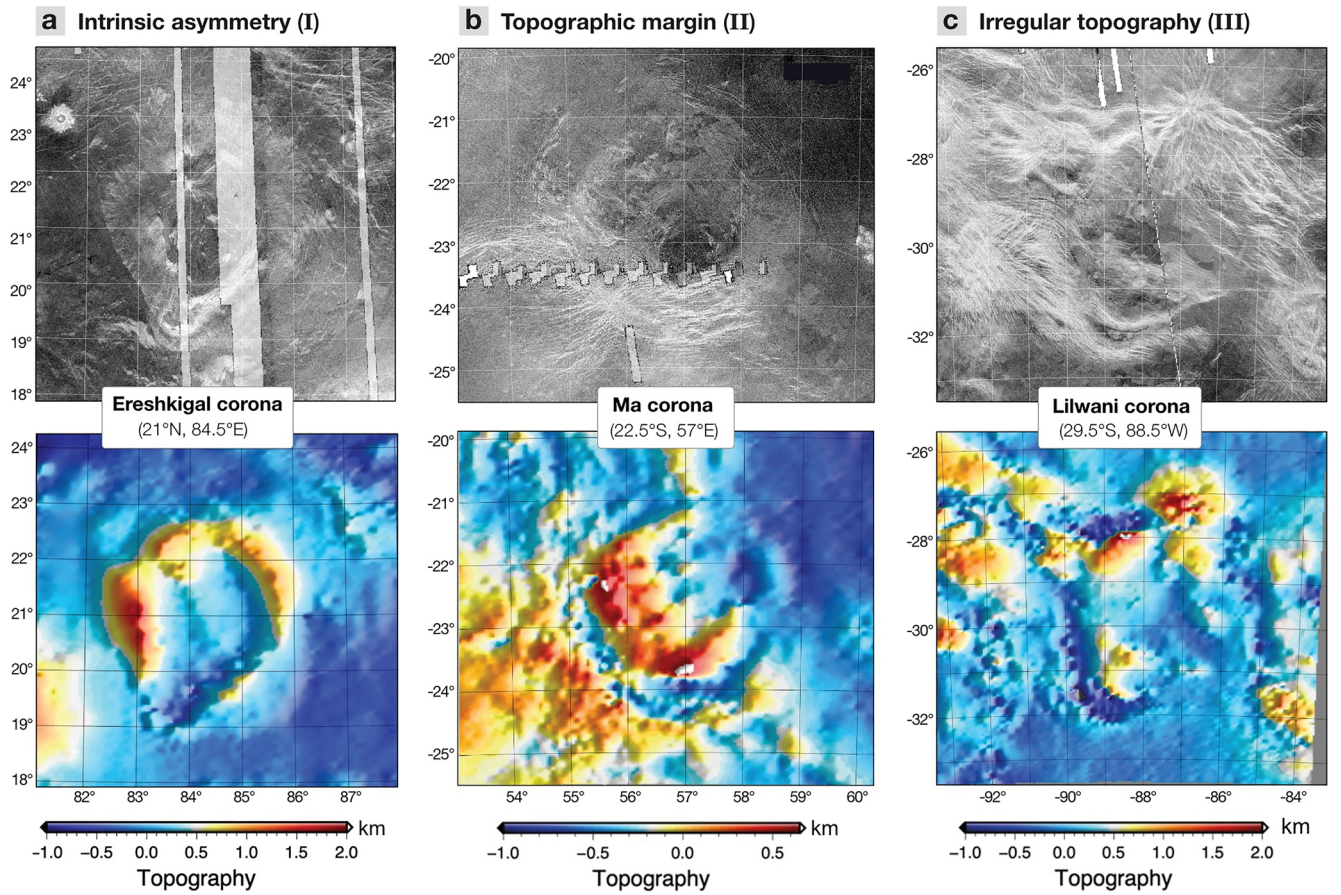

Figure 2. Example of the three sub-classes of asymmetric coronae, showing two data sets from the Magellan mission: the synthetic aperture radar (SAR) imagery at the top and the topography at the bottom. The SAR images combine the Magellan SAR backscatter cycle 1 (left-looking) and cycle 2 (right-looking) data (Pettengill et al., 1991). The topography data (P. G. Ford, 1992) is relative to a mean of 6051.877 km radius. The individual panels are Lambert azimuthal equal-area projections centered around each corona's central coordinates. The sub-classes are defined based on the relation of the asymmetric coronae to their surrounding topography. (a) Intrinsic asymmetry (I): the Ereshkigal corona (21°N, 84.5°E); (b) Topographic margin (II): Ma corona (22.5°S, 57°E). (c) Irregular topography (III): Lilwani corona (29.5°S, 88.5°W). For description of each sub-class, the reader is referred to the main text.

is situated in the Parga Chasma (BAT-region) and is bounded by multiple other coronae, making its boundaries difficult to establish.

Our topographic (a)symmetry classification differs from the SAR-based corona classification of Stofan et al. (1992), which defined the distinguishing characteristic of "asymmetric coronae" for having sinuous to angular annuli, meaning a fracture pattern deviating from circular or elongated. Numerous coronae that are defined "asymmetric" in this study due to a clear variation in topographic profile, do not have an asymmetric classification in Stofan et al. (1992) because they are circular/elongated in planform shape. This is the case for for example, the Ereshkigal corona (Figure 2a).

Our analysis reveals that many asymmetric coronae are located at topographic margins or in complex topographic terrains (see histogram and map in Figure 1), both of which likely represent regions characterized by strong spatial heterogeneity in crustal thickness and/or lithospheric thermal-rheological structure. Many large topographic highlands on Venus are likely supported by crustal thickening (e.g., Grimm, 1994; Smrekar & Phillips, 1991), with crustal thickness estimates ranging from 20 to 50 km compared to a 8–25 average crustal thickness (e.g., James et al., 2013; Jiménez-Díaz et al., 2015; Maia & Wieczorek, 2022). Most topographic highlands seem near-isostatically compensated and linked to thin elastic lithospheric values (Anderson & Smrekar, 2006; Maia & Wieczorek, 2022). There is evidence that crustal plateaus are the oldest (or at least slightly older) terrains on Venus (e.g., Ivanov & Head, 2011), which would be consistent with near-isostatic compensation. Some volcanic rises, such as the Atla, Eistla, and Themis Regio, and Ishtar Terra, are suggested to be (additionally) supported by

dynamic support from the mantle (James et al., 2013; Sandwell et al., 1997; Simons et al., 1997). Note, however, that many of the "topographic coronae" analyzed in this study do not necessarily bound the largest Venusian highlands as classified in Ivanov and Head (2011), as seen in Figure S1 in Supporting Information S1. In the proximity of rift zones on Venus (Figure S1 in Supporting Information S1), crustal and lithospheric thickness is also expected to vary laterally (e.g., Jiménez-Díaz et al., 2015).

For this study we assume that plume-margin interactions on Venus can cause asymmetric coronae to develop. This assumption intrinsically involves the idea that many (asymmetric) coronae on Venus were formed after the formation of lateral changes in lithosphere and crust (e.g., crustal plateaus). It is commonly inferred that coronae emplacement is younger than the formation of the largest highland terrains on Venus (e.g., Ivanov & Head, 2011), whereas the temporal relationship to rift zones is non-unique (Hamilton & Stofan, 1996). With 3D numerical models, we investigate the physical processes behind plume-margin interactions on Venus. The results reveal multiple geodynamic and tectonic regimes that give rise to different types of corona topographies at the surface. The thermal structure of the highlands controls the style of plume-lithosphere interactions, and by that, coronae surface morphology. Finally, we make suggestions on the physical processes responsible for asymmetric coronae on Venus, and ultimately, the planet's geological history.

3. Numerical Methods

3.1. Numerical Method and Model Set-Up

We employ the code I3ELVIS (Gerya, 2010) to model plume-margin interactions in a Venus-like environment. I3ELVIS combines conservative finite differences on a fully staggered grid and marker-in-cell techniques with a multigrid solver (Gerya, 2010; Gerya & Yuen, 2007). The momentum, mass and heat conservation equations are solved on the non-deforming Eulerian grid whereas Properties including temperature, viscosity, melt fraction, and plastic strain are advected on the moving Lagrangian (material) markers in accordance with the velocity field computed on the fixed Eulerian grid. Non-Newtonian viscous-plastic rheologies are used (see next Section), which is also fully thermodynamically coupled and accounts for mineralogical phase changes, adiabatic, radiogenic and frictional internal heating sources. The model dimensions are 1,616 × 392 × 1,616 km, with a uniform rectangular grid of 405 × 196 × 405 nodes (i.e., a uniform grid resolution of 4 × 2 × 4 km) and 130 million randomly distributed Lagrangian markers. All mechanical boundary conditions are free slip except for the lower boundary, which is defined as an open boundary (Ueda et al., 2008). The free surface boundary condition atop the crust is implemented by using a "sticky air" layer (Schmeling et al., 2008).

The initial model setup impinges a thermal mantle plume into a laterally heterogeneous Venusian lithosphere consisting of a topographic lowland linearly transitioning into a plateau (Figure 3). The crust consists of upper crustal material (basalt) over a lower crustal layer (gabbroic rock) similar to oceanic crust on Earth, underneath which lies the thermal lithosphere (lower boundary defined as 1300 K) and the astenospheric mantle. Table 1 lists the material properties that are used in our numerical models. For consistency, we chose these for values to be equal those used in previous studies of plume-lithosphere interactions on Venus (Gülcher et al., 2020). The potential of other crustal rheologies on Venus is discussed in Section 5.5. The Venusian surface gravitational acceleration value of 8.87 $m{\cdot}s^{-2}$ is used in all models. The initial temperature profile in the lithosphere is calculated according to the prescribed lithospheric age (Turcotte & Schubert, 2002) with an additional term for the adiabatic thermal gradient of 0.5 $K{\cdot}km^{-1}$ (as in Gülcher et al., 2020). The lithospheric age in the lowland is set to 40 Myr, corresponding to a thermal lithosphere lower boundary at 47 km depth. We use varying lithospheric ages for the plateau (see Section 3.3). The temperature in the asthenosphere is computed according to the adiabatic thermal gradient of 0.5 $K{\cdot}km^{-1}$. A spherical thermal mantle plume 90 km in diameter is placed at 250 km below the surface. The constant elevated temperature within the plume is set to 1888 K, opposed to the surrounding asthenospheric temperatures of 1650 K (top of the plume) to 1750 K (bottom of the plume). The modeled plume represent a type of "transient" mantle plume (in size and timescale) as described in Johnson (2003); Robin et al. (2007) Our initial set-up, that is, plume buoyancy and lithospheric strengths explored, intrinsically causes the plume to be significantly buoyant and able to (partially) penetrate the Venusian crust in all cases (see Text S2.2 in Supporting Information S1).

3.2. Rheology, Phase Changes, and Melting

Several rock types are considered in both solid and (partially) molten state. The rheological and melting model adopted in our numerical models is equal to that in Gülcher et al. (2020). A constant low Newtonian viscosity of 10^{18} Pa·s

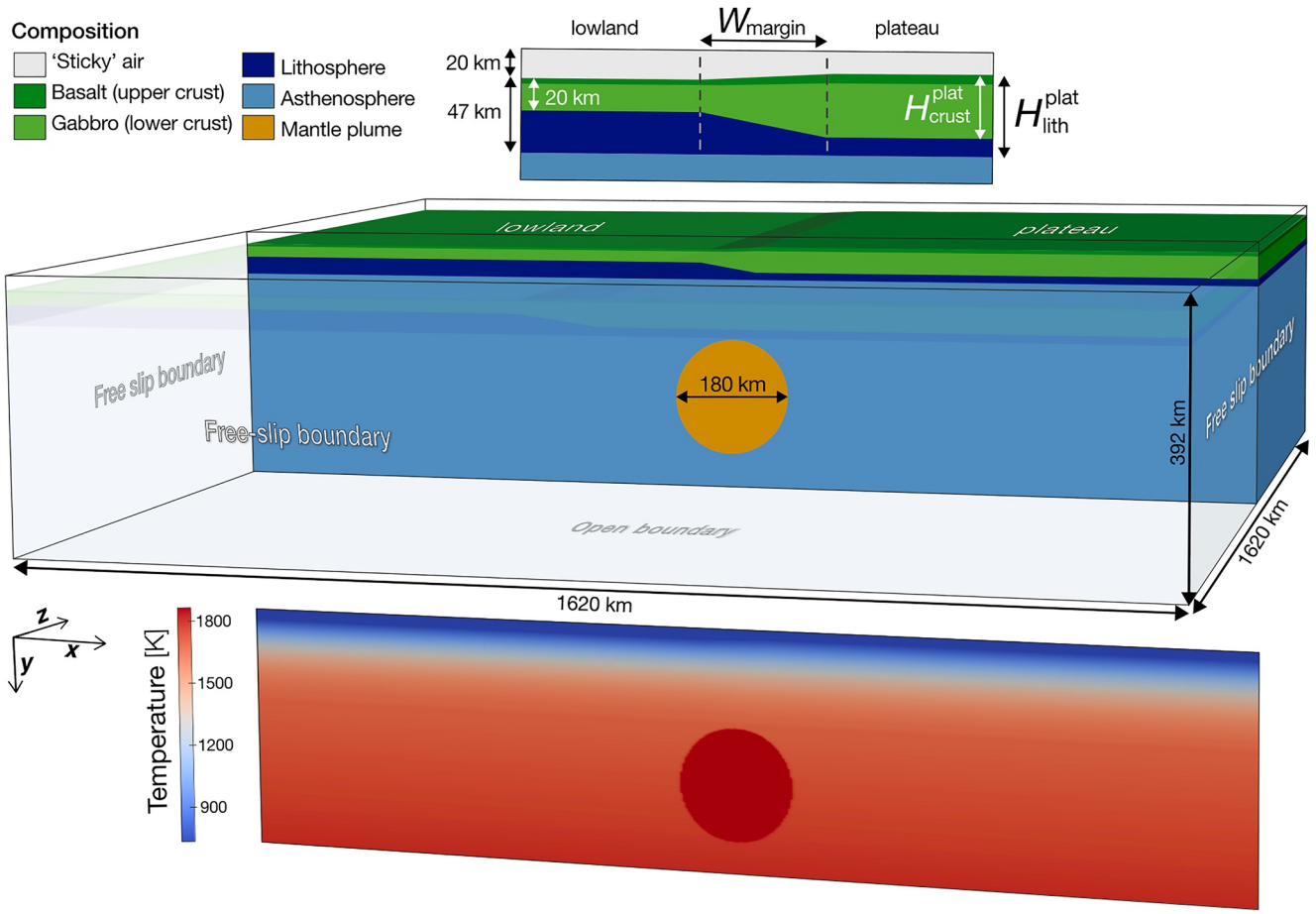

Figure 3. Numerical model design and boundary conditions. A 2D cross-section through the center of the model shows initial composition configuration (upper cross-section) and initial temperature distribution (lower cross-section). The vertical model boundaries in the x and z direction are symmetric. At the top, a zoom-in on the compositional set-up at the topographic margin is given. We investigate several parameters related to the structure of the margin and the plateau: W_{margin}, H^{plat}_{crust}, and H^{plat}_{lith}, see Section 3.3 for more details.

is considered for the partially molten crust and magma extracted from the mantle plume, and a non-Newtonian visco-plastic rheology for the solid crust and mantle based on experimentally determined flow laws (see Table 1). Viscous and plastic behavior are implemented via evaluation of the material's effective viscosity. For ductile rheology, contributions from flow laws of both linear diffusion creep as well as power-law dislocation creep are taken into account via computation of the inverse average ductile viscosity. The different colors for the asthenospheric and lithospheric mantle in the figures of this paper are only for better visualization of the cold slabs/drips. As in Gülcher et al. (2020) and Koptev et al. (2015), strain and melt-induced weakening is assumed for the brittle (plastic) rheology, using a modified Ducker-Prager yield strength criterion defining the visco-plastic rheology transition. A more detailed description of the vico-plastic rheology implementation can be found in Text S2.1 in Supporting Information S1.

Eclogitization of crustal material is implemented as a linear density increase with pressure from 0% to 16% in the pressure–temperature region of garnet-in and plagioclase-out phase transitions in basalt (Ito & Kennedy, 1971) (see Figure S3a in Supporting Information S1). Numerical implementations of slab dehydration and mantle hydration used in former numerical studies on tectonic settings under Earth conditions (Gerya, 2013; Gülcher et al., 2019) are deactivated in the code, as we assume a dry planetary interior for Venus.

Partial melting of the mantle plume, melt extraction and melt percolation toward the bottom of the crust are implemented in a simplified manner. For the crust, the pressure- and temperature-dependent volumetric melt fraction is calculated using an experimentally calibrated batch melting model (Katz et al., 2003). For details regarding the implementation of partially molten materials and melt transport, the reader is referred to Gülcher et al. (2020).

Table 1
Physical Properties of Rock Materials Used in the Numerical Experiments

Material	Initial density ρ_0 (kg/m^3)	Thermal conductivity κ (W/m·K)	Rheology	H_r (μW/m^3)
Upper crust (basalt)	3000 (solid) 2900 (partially molten)	$1.18 + \frac{474}{T+77}$	*Wet quartzite flow law*: $A_d = 1.97 \cdot 10^{17}$, $n = 2.3$, $E = 154$ kJ/mol, $V = 0$ J/mol/MPa, $\sigma_{cr} = 3 \cdot 10^4$ Pa, $C = 0.3$ MPa, $\phi_0 = 0.2$	0.25
Lower crust (gabbro)	3000 (solid) 2900 (partially molten)	$1.18 + \frac{474}{T+77}$	*Plagioclase An75 flow law*: $A_d = 14.8 \cdot 10^{17}$, $n = 3.2$, $E = 238$ kJ/mol, $V = 0$ J/mol/MPa, $\sigma_{cr} = 3 \cdot 10^4$ Pa, $C = 0.3$ MPa, $\phi_0 = 0.2$	0.25
Newly formed crust	3000 (solid) 2900 (partially molten)	$1.18 + \frac{474}{T+77}$	*Plagioclase An75 flow law*: $A_d = 14.8 \cdot 10^{17}$, $n = 3.2$, $E = 238$ kJ/mol, $V = 0$ J/mol/MPa, $\sigma_{cr} = 3 \cdot 10^4$ Pa, $C = 0.3$ MPa, $\phi_0 = 0.2$	0.25
Lithospheric mantle and asthenosphere	3300 (solid) 2900 (partially molten)	$0.73 + \frac{1293}{T+77}$	*Dry olivine flow law*: $A_d = 3.98 \cdot 10^{17}$, $n = 3.5$, $E = 238$ kJ/mol, $V = 8$ J/mol/MPa, $\sigma_{cr} = 3 \cdot 10^4$ Pa, $C = 0.3$ MPa, $\phi_0 = 0.2$	0.022

Note. To allow for comparison with our previous modeling study, we used the same physical properties as in Gülcher et al. (2020). A_d is the material constant, n is the stress exponent parameter, E and V represent activation energy and volume, respectively, σ_{cr} is the diffusion–dislocation creep transition stress, C is material cohesion, ϕ_0 is the internal friction coefficient and H_r is the constant radioactive heating of the material. Flow law for all materials based on Ranalli (1995). All rock materials have the following additional melt-induced weakening parameters: the melt flux needed to be reached for melt-induced weakening $f_{melt,max} = 10^{-10}$ m·s^{-1} and the maximum melt-induced weakening factor $\lambda_{melt,0} = 0.01$ (see Text S2.1 in Supporting Information S1 for description of these parameters). Upper and lower cut-off viscosity limits are set to 10^{24} and 10^{18} Pa·s, respectively.

3.3. Model Parameters Explored

We varied several model parameters related to the initial topographic margin set-up: the change in crustal thicknesses, the presence or absence of thermal lithospheric heterogeneity along the margin, and the transition width of the topographic margin (see Figure 3). The crustal thickness of the lowland is set to 20 km in all models, while that of the crustal plateau $\left(H_{crust}^{plat}\right)$ is varied between 27, 33, and 40 km (i.e., plateau:lowland crustal thickness ratios of 1.35, 1.1.65, and 2). In one set of models, the lithospheric age remains constant across the margin (40 Myr), meaning that heterogeneity is purely compositional across the margin (as illustrated in Figure 3). In a second set of models, thermal heterogeneity accompanies crustal heterogeneity by increasing the lithospheric age of the plateau, resulting in a thicker, colder plateau lithosphere $\left(H_{lith}^{plat}\right)$. For these cases, we determine the plateau age such that the plateau:lowland lithospheric age ratio matches the ratio in plateau:lowland crustal thickness (i.e., 54, 66, and 80 Myr). Such thermal heterogeneity can be expected when considering that crustal plateaus are older features (e.g., Ivanov & Head, 2011). The topographic signature that accompanies the plateau-side is calculated with a simplified airy isostacy assumption, leading to a plateau topography ranging from 640 m to 1.8 km. Within both sets of models, the modeled margin transition zone width W_{margin} varies between 100, 200, and 300 km, with the modeled mantle plume always situated in the center of it (see Figure 3). Finally, for selected cases only, the parametrization of the basalt-to-eclogite phase change (see previous Section) is varied. In these cases, the density increase associated with the phase change is reduced to 90, 80, or 70% of the original value (i.e., to $\triangle\rho_{ecl}$ = +14.4%, +12.8% or +11.2%). These parameter changes are motivated by our limited knowledge of crustal composition on Venus (see review by Gilmore et al., 2017). Overall, we ran 24 different numerical models, their setup conditions are given in Table 2.

4. Modeling Results

In all 3D numerical models of Venusian plume-margin interactions, corona-like structures develop at the surface, most of which are asymmetric in shape. The rising mantle plume penetrates the lithospheric mantle in all cases, yet the subsequent evolution differs between the models. The results reveal that the coronae morphology is directly related to the crustal and lithospheric structure underneath which the thermal mantle plume rises. We found several distinct geodynamic regimes responsible for asymmetric corona formation, described below.

4.1. Geodynamic Regimes of Plume-Margin Interactions on Venus

4.1.1. Lowland-Sided Subduction

Figures 4a–4d show the temporal evolution of a representative model for the lowland-sided subduction regime. The model initially includes a crustal plateau of 40 km thickness, a margin width of 100 km, and no thermal lithospheric step (lower boundary of the thermal lithosphere at 47 km depth throughout the model). The buoyant mantle plume rises toward the surface and its proximity causes the overlying crust to rheologically weaken. Increased temperatures and lithospheric thinning trigger the development of an uplifted crustal dome atop the circular plume head (Figure 4a). The plume enters through the lithosphere and initially pushes material to the side on both directions. Subsequently, it widens toward the lowland-side, where the relatively thinner and colder crust is pushed outwards and downwards by the advancing plume material, producing an outer rise surrounding a deep trench and a still elevated interior (Figure 4b). On the lowland, a short-lived subduction zone develops that retreats into the lowland side, which causes a deep trench to form in the surface topography

Table 2
Model Parameter Summary and Output Quantities of the Numerical Models Run in This Study

Model	H_{crust}^{plat} (km)	age_{lith}^{plat} (Myr)	H_{lith}^{plat} (km)	W_{margin} (km)	T_{moho}^{plat} (K)	F_{L}^{plat} (Pa)	$\triangle F_L/\triangle x$ (Pa·m^{-1})	Geodynamic regime
M40a	40	40	47	100	1236	$2.72 \cdot 10^6$	−1.06	Lowland lith. subduction
M40b	40	40	47	200	1236	$2.72 \cdot 10^6$	−0.53	Trench polarity reversal
M40c	40	40	47	300	1236	$2.72 \cdot 10^6$	−0.35	Trench polarity reversal
M33a	33	40	47	100	1162	$2.76 \cdot 10^6$	−0.69	Lowland lith. subduction
M33b	33	40	47	200	1162	$2.76 \cdot 10^6$	−0.35	Lowland lith. subduction
M33c	33	40	47	300	1162	$2.76 \cdot 10^6$	−0.23	Trench polarity reversal
M27a	27	40	47	100	1092	$2.79 \cdot 10^6$	−0.37	Lowland lith. subduction
M27b	27	40	47	200	1092	$2.79 \cdot 10^6$	−0.19	Embedded plume
M27c	27	40	47	300	1092	$2.79 \cdot 10^6$	−0.12	Embedded plume
Mt40a	40	80	66	100	1113	$3.95 \cdot 10^6$	+11.23	Plateau lith. dripping
Mt40b	40	80	66	200	1113	$3.95 \cdot 10^6$	+5.61	Plateau lith. dripping
Mt40c	40	80	66	300	1113	$3.95 \cdot 10^6$	+3.74	Plateau lith. dripping
Mt33a	33	66	60	100	1080	$3.64 \cdot 10^6$	+8.09	Plateau lith. dripping
Mt33b	33	66	60	200	1080	$3.64 \cdot 10^6$	+4.04	Plateau lith. dripping
Mt33c	33	66	60	300	1080	$3.64 \cdot 10^6$	+2.70	Plateau lith. dripping
Mt27a	27	54	55	100	1050	$3.38 \cdot 10^6$	+5.48	Plateau lith. dripping
Mt27b	27	54	55	200	1050	$3.38 \cdot 10^6$	+2.74	Plateau lith. dripping
Mt27c	27	54	55	300	1050	$3.38 \cdot 10^6$	+1.83	Plateau lith. dripping
M40a^{ecl09}	40	40	47	100	1236	$2.72 \cdot 10^6$	−1.06	Lowland lith. subduction
M40a^{ecl08}	40	40	47	100	1236	$2.72 \cdot 10^6$	−1.06	Lowland lith. subduction
M40a^{ecl07}	40	40	47	100	1236	$2.72 \cdot 10^6$	−1.06	Lowland lith. subduction/Embedded plume
Mt40a^{ecl09}	40	80	66	100	1113	$3.95 \cdot 10^6$	+11.23	Plateau lith. dripping
Mt40a^{ecl08}	40	80	66	100	1113	$3.95 \cdot 10^6$	+11.23	Plateau lith. dripping
Mt40a^{ecl07}	40	80	66	100	1113	$3.95 \cdot 10^6$	+11.23	Plateau lith. dripping

Note. Common parameters across all models are: plume radius and temperature of 90 km and 1888 K, lowland crustal thickness $\left(H_{crust}^{low}\right)$ of 20 km and lowland lithospheric age $\left(age_{lith}^{low}\right)$ of 40 Myr (corresponding to a lowland lithospheric thickness of 47 km and a moho temperature of 1006 K). The models with superscript ^{R} were run with an increased resolution of $2 \times 1.5 \times 2$ km^3, all other models have a resolution of $4 \times 2 \times 4$ km^3 (x·y·z). The first four parameters (H_{crust}^{plat}, age_{lith}^{plat} or H_{lith}^{plat}, and W_{margin}) are the main parameters varied in this study (see Section 3.3). The superscripts $^{ecl07-ecl09}$ stand for an adjusted density increase $\triangle\rho_{ecl}$ related to the basalt-to-eclogite phase change (i.e., 70%, 80%, and 90% of the original value, see Methods and Section 4.3). T_{moho}^{plat} represents the moho temperature of the plateau and F_{L}^{plat} stands for the lithospheric strength of the plateau (see Text S2.2 in Supporting Information S1 for definition). $\triangle F_L/\triangle x$ represents the gradient in lithospheric strength across the margin. Geodynamic regimes: lowland-sided subduction (Section 4.1.1), plateau-sided lithospheric dripping (Section 4.1.2), trench polarity reversal (Section 4.1.3), and embedded plume (Section 4.1.4).

(Figure 4c). Necking of the slab starts in the middle of the subduction arc (Figure 4c) and propagates toward the sides of the arc. For the model M40a displayed in Figures 4a–4d, a period follows of margin-parallel slab retreat by the two slab segments. These slab segments ultimately break off and subduction ceases. This margin-parallel subduction phase creates a highly deformed corona morphology which is elongated parallel to the margin axis (Figure 4d). This margin-parallel subduction and elongation occurs only in the models with the strongest crustal thickness variations (20–40 km) across the margin and in the absence of thermal lithospheric heterogeneity (see Figures S5a–S5c in Supporting Information S1). For all other cases within this regime, the initial necking of the lowland-sided subduction arc occurs fast enough for the corona shape to stay relatively circular. Except for the very first evolution stage (Figure 4a), the corona morphology is radially asymmetric through time.

4.1.2. Plateau-Sided Lithospheric Dripping

When the mantle plume rises toward a topographic margin in which the plateau lithosphere is older, and hence stronger, a different geodynamic regime is displayed (Figures 4e–4h). A lithospheric temperature gradient across the margin makes the lithosphere on the crustal plateau-side relatively more negatively buoyant. When the plume

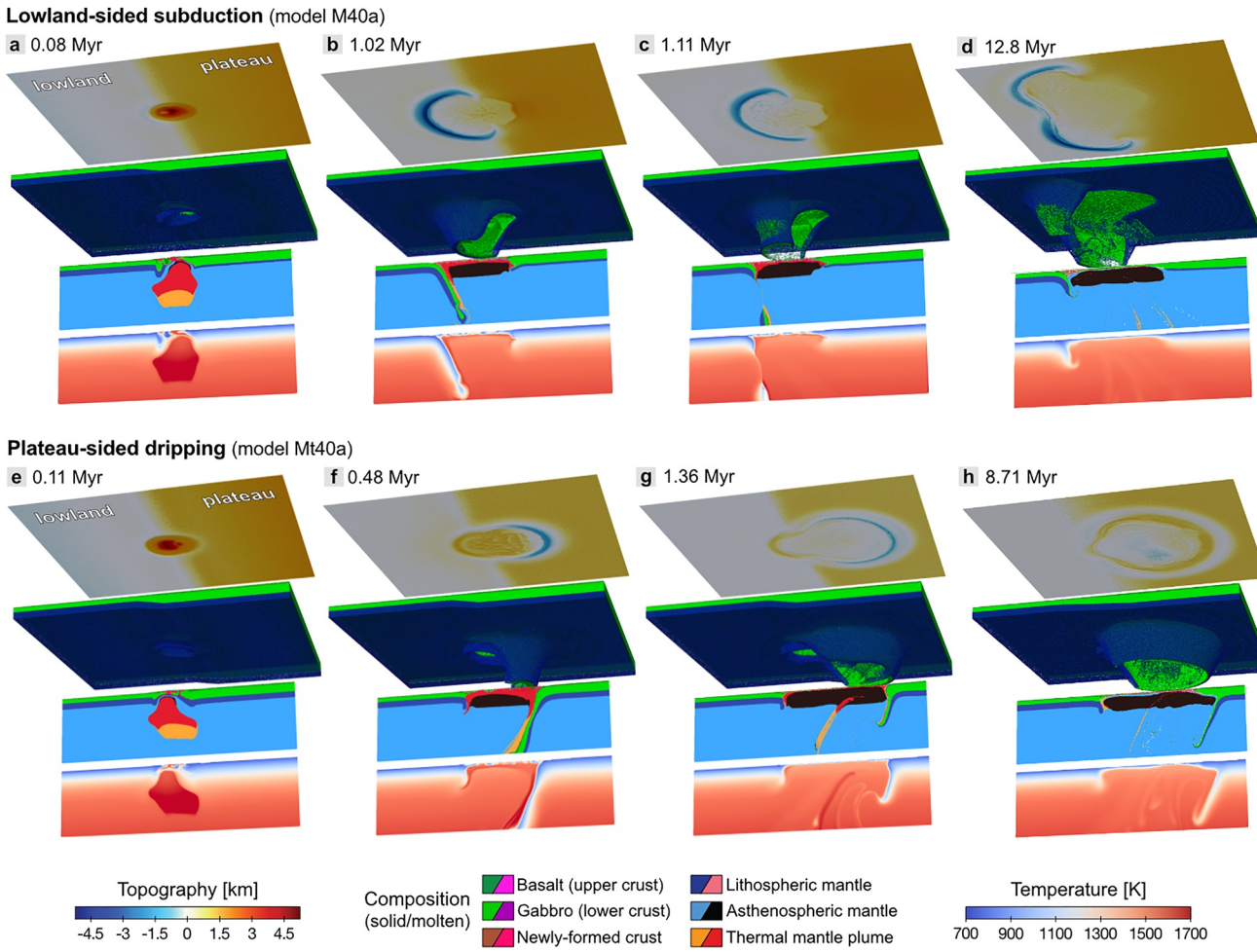

Figure 4. Plume-margin interactions and coronae development in the lowland-sided subduction regime (a–d) and the plateau-sided dripping regime (e–h). Each panel includes a map of surface topography and a cross-section showing composition and temperature fields taken in the center of the model. The dimensions of the panels (1,000 × 300 × 1,000 km) are a zoom-in of the full model domain (1,616 × 392 × 1,616 km). (a–d) In model M40a, with a crustal thickness increase of 20–40 km along a 100 km transition margin (no thermal lithospheric step), a short-lived retreating subduction site at the lowland side causes a trench to deepen and migrate. The subduction episode ceases (slab break-off) at first in the middle of the subduction arc, after which a period of margin-parallel trench retreat follows the initial slab necking. This margin-parallel trench retreat only occurs for the cases with the strongest crustal thickness variation along the margin (20–40 km), as displayed here. (e–f) Results of model Mt40a, the same initial set-up but with a significant increase of lithospheric age (i.e., thickness) from 40 to 80 Gyr across the margin. Multiple sequences of lithosphere dripping occur underneath the plateau. This creates an advancing outer trench in the plateau, which is strongest in models with the largest crustal thickness variations across the margin.

reaches this topographic margin, it is slightly deflected by the cold plateau and instead more easily penetrates through the thinner lithosphere on the lowland-side (Figure 4e). However, as soon as the plume and melt intrusions come near the surface, the plume material advances toward the plateau-side while the negatively buoyant is pushed outwards and downwards. This produces an outer rise surrounding a deep trench and a still elevated interior (Figure 4f). As the plume head widens further, the displaced crust and lithospheric mantle at the plateau side form a lithospheric slab/drip at the plume margin above which a deep trench develops (Figure 4g). As crustal material is soon at high temperatures and -pressures, it densifies due to the basalt-to-eclogite phase change (Methods), causing lithospheric drips to break off and sink into the mantle. Interestingly, the downgoing lithospheric drip also traps hot material in its way down (see e.g., Figure 4f). The subsequent rising of this hot material causes renewed magmatic activity and another episode of lithospheric dripping underneath the plateau. This cycle can repeat itself several times, and is enhanced for models with the most major changes across the topographic margin. The recurrent lithospheric dripping cause the corona structure to advance further into the plateau (Figure 4h).

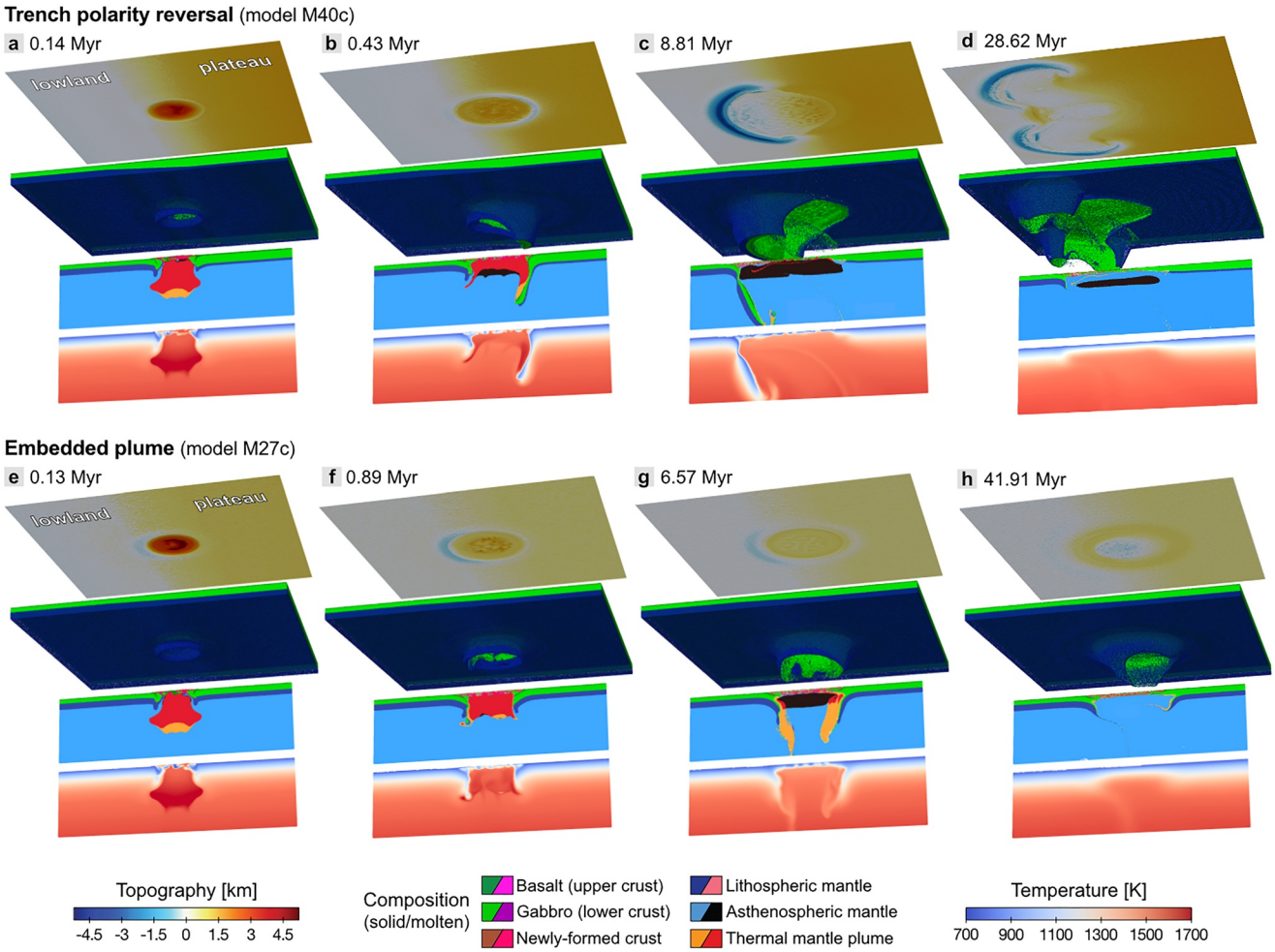

Figure 5. Interior and surface topography development in the "Trench polarity Reversal" regime (a–d) and "Embedded Plume" regime (e–f). In both models, the width of the topographic margin is 300 km wide. The dimensions of the panels (1,000 × 300 × 1,000 km) are a zoom-in of the full model domain (1,616 × 392 × 1,616 km). The panels show fields similar to that in Figure 4. (a–d) Model M40c, which is similar to model M40a shown in Figures 4a–4d except for the wider margin width of 300 km. This regime initially displays a lithospheric drip underneath the plateau, followed by a retreating subducting slab underneath the lowland that ultimately breaks off. (e–f) Model M27c, with the same initial set-up as M40c displayed in panels a–d, but with a smaller crustal thickness variation across the wide margin (20–27 km). Here, the plume stays embedded within the lithosphere and crust and fairly symmetric dynamics occur on both sides of the plume head. For a more detailed description of the dynamics these regimes, the reader is referred to Sections 4.1.3 and 4.1.4 in the main paper.

4.1.3. Trench Polarity Reversal: Plateau-Sided Dripping to Lowland-Sided Subduction

Several models reveal a shift in positioning of the topographic trench from the plateau to the lowland ("polarity reversal"). This reversal is linked to a change in the geodynamic regime during the corona development (see Figures 5a–5d). This occurs particularly for models with a wide topographic margin (see Table 2). At first, the plume penetrates the crust (Figure 5a) and spreads radially outwards, creating a circular lithospheric drip which is smaller underneath the lowland and more sizable underneath the plateau. The difference in lithospheric drip size is reflected in the depth of topographic trenches at the surface (Figure 5a). The larger lithospheric drip underneath the plateau soon experiences densification due to the basalt-to-eclogite phase change (see Figure S3b in Supporting Information S1), causing it to delaminate and drip into the mantle (same dynamics as described in Section 4.1.1). Interestingly, this stage is marked by a symmetric corona pattern at the surface (Figure 5b). As the plume material slowly cools, the plume material progressively moves toward the lowland and an subducting slab arc forms. This marks the stage of lowland-sided subduction (see description in Section 4.1.2; Figure 5c) which is followed by slab break-off with necking starting in the middle of the arc and propagating toward the sides. Similar to described in Section 4.1.1, an episode of margin-parallel subduction and elongation occurs for the models

with the strongest crustal thickness variations across the margin (Figure 5d; Figures S5d–S5f in Supporting Information S1), causing a highly deformed corona structure at the surface.

4.1.4. Embedded Plume

Two cases display an "embedded plume" regime. Here, the topographic margin is wide (200 or 300 km), along which the crustal thickness only changes from 20 km in the lowland to 27 km in the plateau. When the plume impinges upon a such a wide topographic margin with relatively minor crustal thickness changes, the plume stays partially embedded in the lithosphere and crust and does not spread out to one particular direction (Figures 5e and 5f). Instead, crustal and lithospheric materials are only slightly displaced and accumulate around all sides of the plume. Only a thin patch of the lowermost lithosphere delaminates and is recycled back into the mantle. While the interior dynamic processes are fairly symmetric across the margin, the surface expression still shows a much deeper trench on the lowland side (Figure 5g). Ultimately, inactivity and cooling of the system will cause the topographic profile to relax toward an inverted profile (Figure 5d). The regime is similar to the "embedded plume" regime described in Gülcher et al. (2020), although here, more crustal and lithospheric material is displaced outwards and downwards than previously described.

4.2. Influence of Crustal and Lithospheric Configuration

We find that the gradient in lithospheric strength across the topographic margin (see Text S2.2 in Supporting Information S1 for its calculation) and the change in moho temperature exert a major control on the style of plume-margin interactions underneath asymmetric coronae (Table 2). As is summarized in Figure 6, plateau-sided lithospheric dripping consistently develops in the case of a lithospheric strength increase across the margin in combination with a relatively low-to-intermediate plateau moho temperature. This highlights the dominating thermal effect over the compositional effect on the lithospheric buoyancy (e.g., compare model M40a and Mt40a in Figure 4). Within the "plateau-sided lithospheric dripping" regime, a thicker crustal plateau does enhance lithospheric dripping and promotes deeper trench formation, likely because the basalt-to-eclogite phase change is sooner reached (see Figure S3c in Supporting Information S1). A smaller crustal thickness variation and/or broader topographic margin transition width reduces the trench depth and the degree of coronae asymmetry. In the absence of a large thermal heterogeneity across the margin, compositional variations across the topographic margin significantly alter the sign (positive/negative) and gradient in lithospheric strength (i.e., buoyancy) across the margin (see Table 2), causing the slab polarity to occur mostly on the lowland-side (see Figures 4a–4d). The stronger lowland-sided lithosphere (thinner crust) is more prone to being pushed downwards by the advancing mantle plume. The low moho temperature causes a subduction-like episode (straight downward slab at an angle) rather than the lithospheric dripping mechanism to be displaced. This is consistent with findings in Gülcher et al. (2020) that a thin crust is more prone to showcase subduction versus dripping in plume-lithosphere interaction models. For the cases in which the lowland is slightly stronger than the plateau lithosphere (negative $\triangle F_L/\triangle x$ in Figure 6), a smaller crustal thickness change and/or a broader topographic transition width lower the gradient in lithospheric strength across the margin, which in certain cases, significantly alters plume-margin dynamics (e.g., compare models M40a, M40c, and M27c in Figures 4a–4d and 5).

4.3. Influence of the Basalt-To-Eclogite Phase Change

As a final test, we repeated models M40a (lowland-sided subduction) and Mt40a (plateau-sided dripping), displayed in Figure 4), with adjusted phase change parametrizations (a lower $\triangle\rho_{ecl}$, as described in Methods Section 3.2). The results of these test cases are displayed in Figure 7. The density increase associated with the basalt-to-eclogite phase change influences model evolution in several ways. A reduced density increase causes less crustal material to be recycled into the mantle by subduction or dripping. The dynamics become more akin to the embedded plume regime (described in Section 4.1.4. When the density increase across the phase changed is reduced to 11% (w.r.t. $\triangle\rho_{ecl} = 16\%$), only the very lowermost crust is recycled into the mantle (see Figures 7c and 7f). Moreover, the mantle plume evolution is also faster and the depth of the trenches at the surface is significantly reduced for decreasing $\triangle\rho_{ecl}$ values (see trend in Figures 7a–7c and 7d–7f).

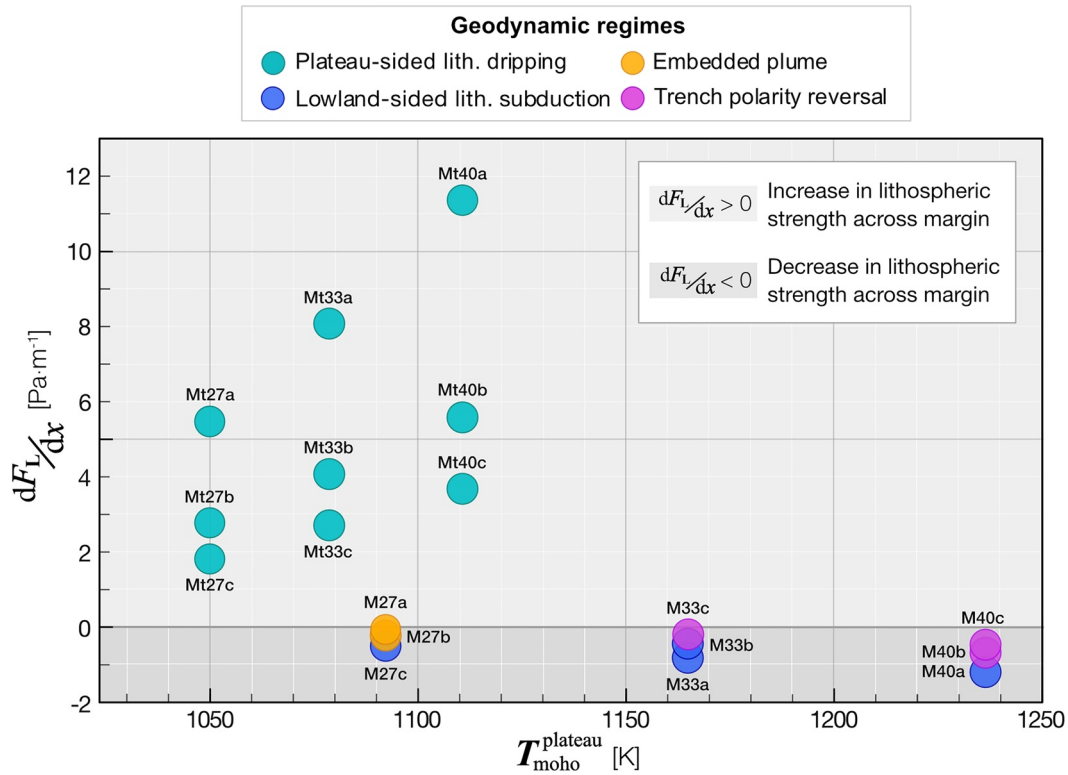

Figure 6. Regime diagram as a function of the gradient across the topographic margin in lithospheric strength (vertical axis, see Suppl Methods for calculations) and the plateau Moho temperature (horizontal axis). Since the lowland moho is kept constant, the plateau moho temperature axis (horizontal axis) is analogous to the change in moho temperature across the margin. The plateau-sided dripping regime is separated from all other regimes by the positive $\triangle F_L/\triangle x$ and a low-to-intermediate change in moho temperature. In the absence of thermal heterogeneity across the margin, $\triangle F_L/\triangle x$ has the opposite sign (negative, dark gray shaded area), meaning that the lowland lithosphere is slightly stronger than the plateau lithosphere. The varied parameters $H_{\text{plat}}^{\text{crust}}$ and $age_{\text{plat}}^{\text{lith}}$ feed into both axes parameters, whereas the margin width W_{margin} only feeds into $\triangle B_r/\triangle x$. We found these choices for axis parameters to separate the geodynamic regimes most clearly. Note that for this main set of models, the basalt-to-eclogite phase change is accompanied by a material density increase of 16% (Ito & Kennedy, 1971), the test cases with a different density increase are described in Section 4.3.

5. Discussion

5.1. Plume-Margin Interactions on (Early) Earth

Our work presents the first 3D plume-margin interaction models in a Venus-like environment. Several findings are consistent with previous work on modeling plume-plateau interactions under Earth-like conditions (see e.g., review in Cloetingh et al., 2021). In our models, the appearance of either a plateau-sided or a lowland sided trench is similarly dependent on lithospheric configuration (age, crustal thickness, rheological strength), as found in prior studies (e.g., Baes et al., 2020; François et al., 2018). An older plateau lithosphere consistently promotes plateau-sided trench formation also under Earth-like conditions (Baes et al., 2020). A key difference is that the lithospheric recycling dynamics underneath plateau-sided trench formation is consistently subduction for the Earth case (i.e., a relatively colder, stiffer lithosphere as for Venus). In our numerical plume-margin models, the relatively hotter, thin, and weak lithosphere causes (repeated) lithospheric dripping to be the style of lithospheric recycling underneath plateau-sided trenches. Plume-margin interactions under hot Archean Earth-conditions were also investigated in 2D numerical studies (Gorczyk et al., 2018) and did reveal the occurrence of lithospheric drips. The numerical technique, and initial set-ups and resolutions, used here differs substantially to those used in previous modeling efforts of plume–margin interactions on Earth (Baes et al., 2020; François et al., 2018; Gorczyk et al., 2018). Therefore, we should take caution in directly comparing the results of previous studies with ours.

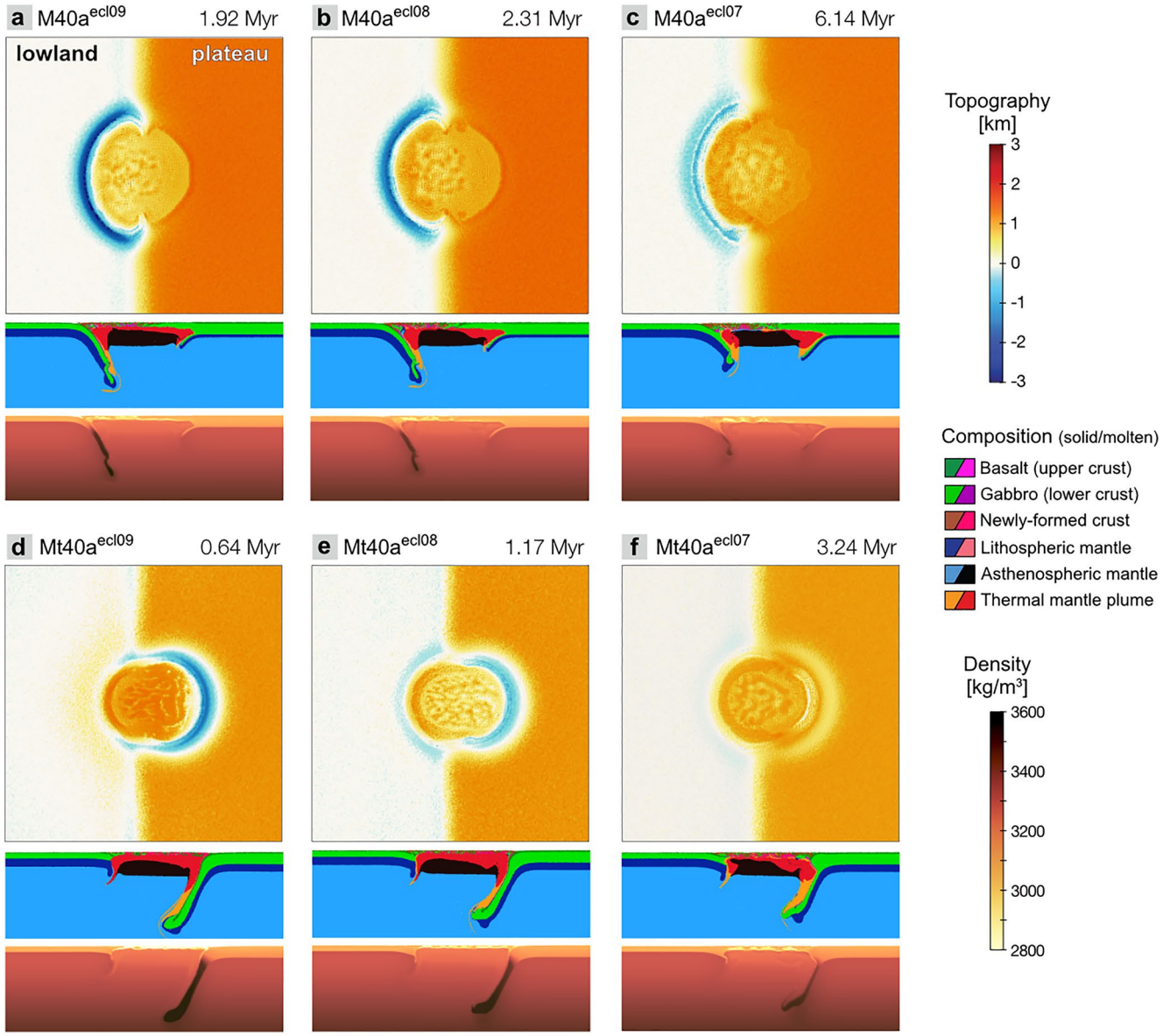

Figure 7. Snapshots of the repetitions of models M40a (Figures 4a–4d) Mt40a (Figures 4e–4h) with adjusted values for the basalt-to-eclogite density increase $\triangle\rho_{ecl}$ ((a–c) and (d–f), respectively), as described in Methods Section 3.2). The dimensions of the panels (1,000 × 300 × 1,000 km) are a zoom-in of the full model domain (1,616 × 392 × 1,616 km). The snapshots were chosen such that the dynamics displayed are as similar as possible (i.e., lowland-sided subduction (a–c) and plateau-sided dripping (d–f)). For a smaller density increases associated with the basalt-to-eclogite phase change (from left to right for lower $\triangle\rho_{ecl}$), a smaller amount of crust is recycled into the mantle and the surface trenches are shallower.

Our results are consistent with the idea that for a cooling early Earth, the tectonic expressions of plume-lithosphere interactions could change from lithospheric dripping to subduction (e.g., Baes et al., 2021, and references therein). Additionally, our work indicates that lithospheric break-up is strongly promoted by lateral changes in lithospheric configuration. When a buoyant plume interacts with a narrow margin across which crustal and/or lithospheric structure more drastically changes, asymmetry and lithospheric recycling is promoted. The presence of narrow and sharp lateral heterogeneities could therefore have played an important role in the initiation of subduction in the Early Earth and, potentially, at the present-day. Indeed, several localities have been proposed to host one-sided subduction linked to plume-margin interactions, such as the Southern Neotethys subduction (between the African and the Eurasian plates) in the Late Cretaceous (Rodriguez et al., 2021), the Cascadia subduction zone located in the Pacific Northwest of North America (Stern & Dumitru, 2019), and the Western Shandong Terran, located in the southeastern margin of the North China craton (Gao et al., 2019).

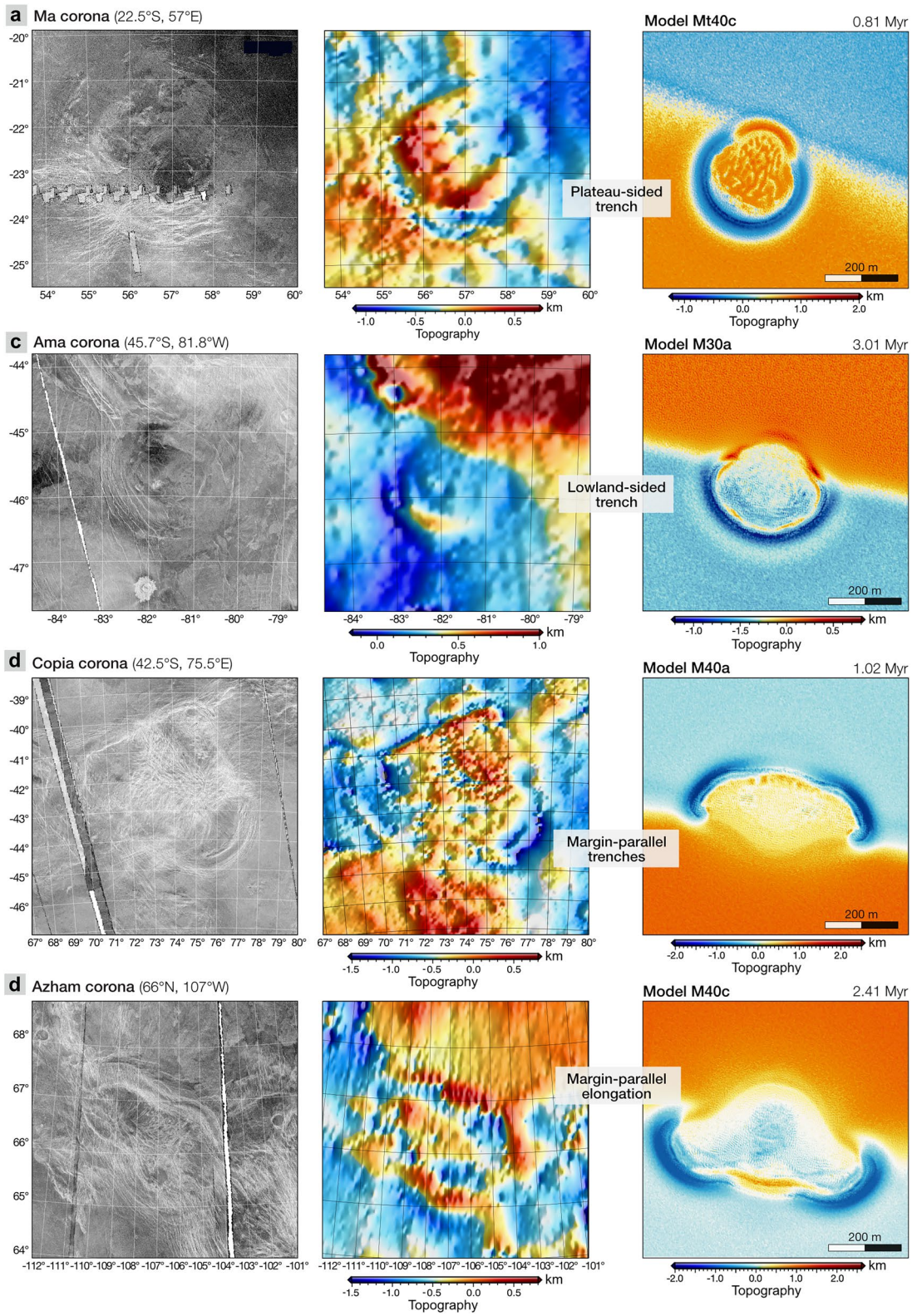

Figure 8. Comparison of corona observation and models. The left two panels show the synthetic aperture radar (SAR) imagery and the topography data from the Magellan mission with a Lambert azimuthal equal-area projections centered around each corona's central coordinates. The SAR images combine the Magellan SAR backscatter cycle 1 (left-looking) and cycle 2 (right-looking) data (Pettengill et al., 1991). The topography data (P. G. Ford, 1992) is relative to a mean of 6051.877 km radius. The right panels are topography snapshots of particular models run in this study. Individual features of observed coronae that are reproduced in our models are highlighted as text.

5.2. (A)symmetric Coronae on Venus

A wide range of features displayed by various asymmetric coronae at topographic margins on Venus are reproduced by the numerical models presented in this study. This includes the occurrence of a plateau-sided trench (displayed by e.g., the Ma and Beyla coronae, see Figures 8a and 8b) as well as a lowland-sided trench (displayed by e.g., the Ama corona, Figure 8c). Moreover, the occurrence of coronae with shapes deviating from perfectly circular, such as the Copia and Azham coronae (see Figures 8d and 8e) is reproduced in many of the models shown here. Especially the corona elongation and magmatic migration related to margin-parallel slab retreat in our models (Figures 8c and 8d) may be relevant for coronae defined as "multiple" in Stofan et al. (1992). Finally, the presence of a double trench (Figure S6 in Supporting Information S1), as also noted in our previous work (Gülcher et al., 2020), is observed at several coronae, such as at the southeastern arc of the impressive Artemis corona (see Extended Data Figure 7 in Gülcher et al. (2020)).

Out of the 48 coronae classified as "topographic margin," we can confidently identify 14 coronae (29%) that display a plateau-sided trench, 6 coronae (15%) that display a lowland-sided trench only, and 3 coronae (6%) that display two opposite and margin-parallel trenches. The higher occurrence of coronae with plateau-sided trenches could suggest that most topographic plateaus linked to crustal roots are relatively older (colder) regions than the lowlands (as suggested by e.g., Ivanov & Head, 2011). However, as some coronae display lowland-sided trenches instead, the lithospheric structure of lowlands versus plateaus is likely non-uniform across the planet. The resolution of the topography data is sometimes too poor to confidently identify individual topographic structures in several coronae. This is particular the case for coronae situated in high latitude regions such as those situated near the margin of Ishtar Terra and Lada Terra (see Figure S1 in Supporting Information S1). Moreover, even if relatively well resolved by topography data, many coronae display more internal complexities than modeled here. Future high-resolution SAR and topography from, for example, EnVision and VERITAS missions will be key in deciphering the detailed structures of Venusian coronae. Finally, the USGS Planetary Nomenclature data set (U.S. Geological Survey, 2023) and the data set provided by Stofan et al. (1992) only encompass about 360 coronae on Venus, while over 500 of them have been identified. There is a need for a publicly available and complete database that integrates the variable available corona lists (e.g., Gülcher et al., 2020; Smrekar & Stofan, 1999; Stofan et al., 1992, 1995).

In most models run in this study, the trenches at the surface are several kilometers deep (especially for lowland-sided subduction and plateau-sided dripping regimes). This is much larger than the trench depths at most coronae on Venus. As discussed in Section 4.3, a slightly different implementation of basalt-to-eclogite phase change affects trench depth (lower density increase reduces trench depth) or can even cause the dynamic regime to shift to an embedded plume with trench roll-back by advancing plume material and inhibit crustal/lithospheric recycling into the mantle. This highlights the importance of better understanding the basalt-to-eclogite phase change in crustal material on Venus and its possible relationship to Venus' resurfacing styles and tectonics.

We classified about 7% of analyzed coronae (9 out of 155) as radially symmetric and situated at a topographic margin. Examples include the circular Aramaiti (26.3°S, 92°E) and Thouris (6.5°S, 12.9°E) coronae. Symmetric coronae at topographic margins are only a transient feature in a few models in our study (see Section 4.1). The radially symmetric features of the Aramaiti corona, such as outer trench, rim, inner depression and dome (see Figure S2b in Supporting Information S1) are best reproduced during a short phase of plume head widening in the embedded plume or trench polarity reversal regimes (Figures 5b and 5f). This suggests that, if our models are applicable to the formation of Aramaiti, the corona is currently in a (transient) active stage, which is in agreement with previous suggestions (Gülcher et al., 2020; Russell & Johnson, 2021). Alternative possible interpretations of symmetric coronae at topographic margins include plateau formation occurring subsequent to the formation of coronae, and/or the coronae being completely inactive (such as suggested for the Thouris corona, which features an outer rim and inner depression, similar to the final model stage in Figure 5h).

5.3. Plume-Induced Resurfacing Styles and Eclogite-Driven Crustal Recycling on Venus

Our results reveal several distinct styles of plume-lithosphere interactions responsible for asymmetrical corona at the surface, highlighting the various styles of plume-induced resurfacing possible for Venus. The variety of corona features observed on Venus as well as reproduced in our models highlights that likely, the formation

scenario of large coronae on Venus is non-unique and a wide range of crustal recycling dynamics could be connected to large coronae.

The tendency for an embedded plume scenario to occur for (a) wider topographic margins or (b) smaller density increase related to the basalt-to-eclogite phase transition highlights the importance of these parameters for regional-scale resurfacing of the Venusian surface. For the topographic margin width, this is particularly evident in the shift from lowland-sided subduction to embedded plume dynamics for increasing margin widths (Figures 5 and 6, Table 2). Moreover, stronger lateral differences across topographic margins extend the longevity of magmatic and tectonic activity (see next Section). Better knowledge on the lateral variability in crustal and lithospheric thickness are therefore crucial to better understand the type of plume-induced crustal recycling styles and tectonic/magmatic longevity. Our results further show the importance of better understanding the basalt-to-eclogite phase change and the composition (as well as its lateral variability) of Venus' crust. The negative buoyancy force coming from the densified slab/drip material due to the basalt-to-eclogite phase change seems key in its ability to sink down into the lithosphere. Along with the slight negative buoyancy of the cold lithosphere, it provides the necessary driving force for the sinking of slab/drips. While the parametrization of eclogitization in our numerical code (described in Text S2.3 in Supporting Information S1) is fairly simple, the transformation of basaltic rocks (e.g., basalt, gabbro, blueschist, amphibolite) into eclogite is a complex process that involves several net-transfer and Fe-Mg exchange mineral reactions studied experimentally (e.g., Cheng & Jenkins, 2021; Griffin, 1972; Zhang & Liou, 1997), which is complex to translate to geodynamical software. While the eclogite phase change has been studied numerically in relation to (early) Earth geodynamics (e.g., Perchuk et al., 2023; Van Hunen et al., 2004), it remains a future target to shed light on its relationship to Venus geodynamics.

Finally, our results reveal several scenarios of plume-margin interactions on Venus under which slab-break off or lithospheric dripping occurs (e.g., Figures 4 and 5). These major tectonic events are related to rapid topographic changes (Gülcher et al., 2020) and surface deformation. Drawing a parallel to Earth, slab break-off or dripping could potentially be a source of seismicity, since the necking of subducting slabs has been proposed to cause major Earthquakes on Earth, such as in the Hindu Kush area in Central and South Asia (e.g., Kufner et al., 2021; Zhan & Kanamori, 2016). It remains a target for future research to assess the potential and expected magnitude of seismicity on Venus in such tectonic settings.

5.4. Prolonged Tectonic and Magmatic Activity of Asymmetric Coronae on Venus

A significant conclusion from our results is that the tectonic and magmatic lifetime of coronae are greatly enhanced by larger gradients of lithospheric/crustal properties across topographic margins. The magmatic (i.e., presence partially molten crustal intrusions) and tectonic (active plume head widening and/or lithospheric dripping/subduction) lifetime of most models in our paper is at least 20 Myrs (Figures 4 and 5), which is significantly longer than corona activity lifetimes found in prior symmetrical plume-lithosphere interactions models (Gülcher et al., 2020) (mostly <5 Myrs of magmatic and tectonic activity). Lateral crustal/lithospheric variations can therefore prolong the lifetime of plume-induced tectonics and magmatism, alongside other mantle plume-related factors such as a large buoyancy of the mantle plume, a plume tail, or multiple plumes, as has been previously suggested (e.g., Ernst & Desnoyers, 2004; Harris & Bédard, 2014; Jellinek, 2002; Rolf et al., 2022). Several terrestrial studies link lithospheric heterogeneity to intraplate surface volcanism. In particular, the "edge-driven convection" theory involves the interaction of a gradient in lithospheric thickness with the underlying mantle. A convection cell may be generated due to the juxtaposition of two lithospheric sections of different age or structure, causing an upwelling return flow that facilitates decompression melting (e.g., Duvernay et al., 2021; King & Anderson, 1998; Vogt, 1991). Edge-driven convection may also be linked to a nearby upwelling mantle plume, which has been suggested to be the cause of volcanic activity on several places on Earth such as the Colorado Plateau in North America (e.g., Van Wijk et al., 2010), the Moroccan Atlas Mountains in northern Africa (e.g., Kaislaniemi & Van Hunen, 2014), the Newer Volcanics Province of southeastern Australia (e.g., Jennings et al., 2023), and even secondary volcanism away from the Hawaiian hotspot (Ballmer et al., 2011). Based on our numerical simulations, and supported by the above-mentioned studies, we suggest that asymmetrical coronae are generally more long-lived than symmetric coronae.

5.5. Limitations and Future Work

Many exciting scientific avenues can be undertaking in the aftermath of this work. First, several unexplored parameter ranges with respect to crustal rheology and composition could be explored. Although we did not explore the effect of crustal rheology on model evolution, the crustal composition and rheology is far from known for Venus and likely varies laterally (e.g., Elkins-Tanton et al., 2007; Gilmore et al., 2017; Surkov et al., 1984). It would, for example, be interesting to further explore the effect of lateral compositional variability. Crustal material constituting the tessera highlands may be more felsic than the basaltic lowlands on Venus, and even the tesserae themselves seem to show compositional variability (e.g., Brossier & Gilmore, 2021; Gilmore et al., 2017; Hashimoto et al., 2008). We note, however, that only part of the large coronae we analyzed lie at the margin of tesserae, and that many also lie near smaller-scale highlands (see Figure S1 in Supporting Information S1). If compositional variability is accompanied by density differences, our initial assumption of Airy isostacy (see Methods) may need to be revisited. Lateral variability in crustal composition is further expected on Venus as the sinking of compositionally dense lithospheric material allows the formation of a variety of magmatic source regions (and therefrom forming lavas) with different compositions and viscosities (Elkins-Tanton et al., 2007). A felsic plateau may, in our numerical modeling case, lower the strength of the plateau, thereby potentially changing the tectonic styles (see Figure 6). Since our models show the dominance of thermal variability effects on geodynamic styles, it would be interesting to test the role of compositional variability in the presence of thermal lithospheric variability across the topographic margin. One may also explore the effect of a stronger crustal rheology (as proposed by e.g., Nimmo & Mackwell, 2023). We expect that stronger crustal rheology may promote plume-lithosphere interaction styles such as an underplating or embedded plume, as described in Gülcher et al. (2020) and Section 4.1.4.

Moreover, limitations of our employed models can be addressed and improved. The adopted melt-induced weakening (see e.g., Gülcher et al., 2020) does not precisely reflect the physics involved in the various weakening/healing processes, such as melt percolation and grain damage or growth. Further theoretical development and numerical implementation of a more sophisticated and realistic lithospheric weakening/healing model is needed. Apart from the assumptions in the initial model set-up promoting a relatively rapid evolution of the models, the code assumption of instantaneous melt percolation toward the crust further results in an overestimation of the speed at which the plume penetrates through the lithosphere. Moreover, the large-scale visco-plastic rheological model of the lithosphere is simplified and does not account for rock elasticity and damage processes, nor does it account for (partial) healing of deactivated fractures (Gerya, 2013). The Eulerian grid used in most of the experiments is discretized in cells that represent a volume of $4 \times 2 \times 4$ km^3, which precludes the analysis of small-scale localized shear zones. Higher-resolution models would be needed to assess more detailed tectonic features displayed by individual coronae on Venus.

Our numerical models suggest the existence of several potentially detectable processes related to active plume-lithosphere interactions ("active coronae" in Gülcher et al. (2020), and in this paper) for forthcoming Venus missions. These features include - but are not limited to - enhanced crustal degassing and elevated heat fluxes, rapid surface deformation, intense surface and subsurface fracturing, and, potentially, seismic activity (see previous Sections). Based on our numerical experiments, we propose focused targeting of coronae-dominated surface areas by the EnVision (European Space Agency, 2021) and VERITAS (Smrekar et al., 2022) missions, which can critically advance our understanding and quantification of yet enigmatic mantle plume penetration and coronae formation processes. In particular, (Interferometric) Synthetic Aperture Radar instruments aboard the missions can sense details of surface and subsurface fracturing and deformation related to rapid corona topography evolution. Moreover, there is high potential for detecting volcanic activity (active magma outpouring and outgassing) by VenSpec (EnVision) and the Venus Emissivity Mapper (VERITAS) spectrometers, as our numerical models suggest that melt intrusions may come very close to the surface during active corona phases.

6. Conclusions

We present a joint study of mission data analysis and 3D modeling of asymmetric coronae structures on Venus. We provide a classification of 155 large coronae on Venus in terms of surface topography and morphology. We establish that 75% of those coronae are radially asymmetric, and further sub-categorize them based on their adjacent topography. This analysis reveals that many asymmetric coronae are positioned in a region of laterally varying topography. With state-of-the-art 3D numerical models, we investigate the formation of asymmetrical coronae by the interaction of a buoyant mantle plume and a lithosphere transitioning from a lowland to a plateau

(termed "topographic margin"). We find that several tectonic styles may be responsible for asymmetric coronae at topographic margins, which are majorly controlled by the gradient in lithospheric strength across the topographic margin and the density increase related to the basalt-to-eclogite phase change. When the lithospheric strength decreases across the topographic margin (from lowland to plateau), the plume either penetrates through the lithosphere and causes a lowland-sided subduction zone and trench at the surface, or the plume stays embedded within the lithosphere. Alternatively, for an increase of lithosphere strength across the margin (e.g., for an older plateau lithosphere), models consistently show plateau-sided lithospheric dripping which causes a curved trench to form at the plateau-side. We also find that larger gradients of lithospheric strength across the topographic margin enhance the tectono-magmatic lifetime of the corona structures. Finally, we find that the negative buoyancy of the crust caused by the basalt-to-eclogite phase change, along with extra gravitational force coming from the overriding plume material on the lithosphere, provides the necessary driving force for lithospheric dripping or subduction. Therefore, the density increase associated with the basalt-to-eclogite is a major factor controlling the volume of crustal material that is recycled into the mantle via lithospheric dripping/subduction as well as the corona trench depth at the surface. The models presented in this study reproduce a wide set of asymmetrical corona features found on Venus and suggest that they are more long-lived structures than symmetrical coronae. These outcomes aid our understanding of the types of plume-lithosphere interactions and resurfacing styles possible on Venus and, possibly, the early Earth.

Data Availability Statement

Our newly presented corona classification is publicly available on Zenodo (Gülcher, 2023). A full description of this database can further be found in Text S1.1 in Supporting Information S1. Data acquired by the Magellan mission is accessible on the Planetary Data System (PDS) Geosciences Node Venus Orbital Data Explorer (http://ode.rsl.wustl.edu/venus/index.aspx, last access: 15 May 2021). The SAR backscatter cycle 1 (left) and cycle 2 (right) from the Magellan mission (Pettengill et al., 1991) were combined in the software arcGIS to create the panels in Figures 2 and 8; Figure S2 in Supporting Information S1. The gridded topography data (P. G. Ford, 1992) was retrieved from Sandwell (2015) and the open-source software package Generic Mapping Tools (Wessel & Luis, 2017) was used for visualization thereof. This Magellan topography data set has a horizontal resolution of 10–25 km, and a nominal vertical resolution of 80 m (P. G. Ford, 1992). The numerical code along with the input files for the models presented in this study, that allow for reproduction of the numerical results, are provided on Supporting Information S2. The informative text about the code and the input files are found in the README.md files in the folders and also in Texts S3.1 and S3.2 in Supporting Information S1.

Acknowledgments
For this research, A. Gülcher has mainly been supported by the ETH Zürich Research Commission (Grant 636 no. ETH-33 16-1), with additional support by the SNSF Postdoc Mobility Grant P500PN_210729 for the time period of the review process of this paper. T.-Y. Yu was supported by the Thinkswiss Research Scholarship 2022 from the Swiss Government throughout the summer of 2022. All numerical simulations were performed on ETH Zürich's Euler cluster. For 2D and 3D visualisation of the models, we used the open-source software ParaView (http://paraview.org, last access: 20 June 2023). Several perceptually uniform scientific color maps (Crameri, 2018) were used to prevent visual distortion of the figures. We thank Dr. Bradley Thompson for editing this manuscript, and Dr. Megan B. Russel and one anonymous reviewer for their constructive comments that helped to improve the manuscript. Finally, we thank Dr. Suzanne Smrekar (Jet Propulsion Laboratory, California Institute of Technology) for discussions and valuable insights related to this study.

References

Adams, A. C., Stegman, D. R., Smrekar, S. E., & Tackley, P. J. (2022). Regional-scale lithospheric recycling on Venus via peel-back Delamination. *Journal of Geophysical Research: Planets*, *127*(10), e2022JE007460. https://doi.org/10.1029/2022JE007460

Anderson, F. S., & Smrekar, S. E. (2006). Global mapping of crustal and lithospheric thickness on Venus. *Journal of Geophysical Research: Planets*, *111*(8), 1–20. https://doi.org/10.1029/2004JE002395

Baes, M., Sobolev, S. V., Gerya, T., & Brune, S. (2020). Subduction initiation by plume-Plateau interaction: Insights from numerical models. *Geochemistry, Geophysics, Geosystems*, *21*(8), e2020GC009119. https://doi.org/10.1029/2020GC009119

Baes, M., Stern, R. J., Whattam, S., Gerya, T. V., & Sobolev, S. V. (2021). Plume-induced subduction initiation: Revisiting models and observations. *Frontiers in Earth Science*, *9*, 766604. https://doi.org/10.3389/feart.2021.766604

Ballmer, M. D., Ito, G., Van Hunen, J., & Tackley, P. J. (2011). Spatial and temporal variability in Hawaiian hotspot volcanism induced by small-scale convection. *Nature Geoscience*, *4*(7), 457–460. https://doi.org/10.1038/ngeo1187

Bjonnes, E. E., Hansen, V. L., James, B., & Swenson, J. B. (2012). Equilibrium resurfacing of Venus: Results from new Monte Carlo modeling and implications for Venus surface histories. *Icarus*, *217*(2), 395–410. (ISBN: 9781931971874). https://doi.org/10.1016/j.icarus.2011.03.033

Borrelli, M. E., O'Rourke, J. G., Smrekar, S. E., & Ostberg, C. M. (2021). A global survey of lithospheric flexure at steep-sided domical volcanoes on Venus reveals intermediate elastic thicknesses. *Journal of Geophysical Research: Planets*, *126*(7),e2020JE006756. https://doi.org/10.1029/2020JE006756

Brossier, J., & Gilmore, M. S. (2021). Variations in the radiophysical properties of tesserae and mountain belts on Venus: Classification and mineralogical trends. *Icarus*, *355*, 114161. https://doi.org/10.1016/j.icarus.2020.114161

Campbell, B. A., Morgan, G. A., Whitten, J. L., Carter, L. M., Glaze, L. S., & Campbell, D. B. (2017). Pyroclastic flow deposits on Venus as indicators of renewed magmatic activity. *Journal of Geophysical Research: Planets*, *122*(7), 1580–1596. https://doi.org/10.1002/2017JE005299

Cheng, N., & Jenkins, D. M. (2021). Experimental study of metamorphic reactions and dehydration processes at the blueschist–eclogite transition during warm subduction. *Journal of Metamorphic Geology*, *39*(1), 39–56. https://doi.org/10.1111/jmg.12560

Cloetingh, S., Koptev, A., Kovács, I., Gerya, T., Beniest, A., Willingshofer, E., et al. (2021). Plume-induced sinking of intracontinental lithospheric mantle: An overlooked mechanism of subduction initiation? *Geochemistry, Geophysics, Geosystems*, *22*(2), e2020GC009482. https://doi.org/10.1029/2020GC009482

Crameri, F. (2018). Scientific colour-maps. https://doi.org/10.5281/zenodo.1243862

Davaille, A., Smrekar, S. E., & Tomlinson, S. (2017). Experimental and observational evidence for plume-induced subduction on Venus. *Nature Geoscience*, *10*(5), 349–355. https://doi.org/10.1038/ngeo2928

D'Incecco, P., Müller, N., Helbert, J., & D'Amore, M. (2017). Idunn Mons on Venus: Location and extent of recently active lava flows. *Planetary and Space Science*, *136*, 25–33. https://doi.org/10.1016/j.pss.2016.12.002

Duvernay, T., Davies, D. R., Mathews, C. R., Gibson, A. H., & Kramer, S. C. (2021). Linking intraplate volcanism to lithospheric structure and asthenospheric flow. *Geochemistry, Geophysics, Geosystems*, *22*(8), e2021GC009953. https://doi.org/10.1029/2021GC009953

Elkins-Tanton, L. T., Smrekar, S. E., Hess, P. C., & Parmentier, E. M. (2007). Volcanism and volatile recycling on a one-plate planet: Applications to Venus. *Journal of Geophysical Research: Planets*, *112*(4), 1–15. https://doi.org/10.1029/2006JE002793

Ernst, R., & Desnoyers, D. (2004). Lessons from Venus for understanding mantle plumes on Earth. *Physics of the Earth and Planetary Interiors*, *146*(1–2), 195–229. https://doi.org/10.1016/j.pepi.2003.10.012

Esposito, L. W. (1984). Sulfur dioxide: Episodic injection shows evidence for active Venus volcanism. *Science*, *223*(4640), 1072–1074. https://doi.org/10.1126/science.223.4640.1072

European Space Agency. (2021). EnVision: Understanding why Earth's closest neighbour is so different, assessment study report (Tech. Rep.). (Issue: February).

Filiberto, J., Trang, D., Treiman, A. H., & Gilmore, M. S. (2020). Present-day volcanism on Venus as evidenced from weathering rates of olivine. *Science Advances*, *6*(1), eaax7445. https://doi.org/10.1126/sciadv.aax7445

Ford, J. P., Plaut, J. J., Weitz, C. M., Farr, T. G., Senske, D. A., Stofan, E. R., et al. (1993). Guide to Magellan image interpretation. JPL Publication 93-24, 45–56 Retrieved from http://web.archive.org/web/19990420173536/

Ford, P. G. (1992). MGN V RDRS 5 global data record topographic V1.0 [Dataset]. NASA Planetary Data System. https://doi.org/10.17189/1522522

François, T., Koptev, A., Cloetingh, S., Burov, E., & Gerya, T. (2018). Plume-lithosphere interactions in rifted margin tectonic settings: Inferences from thermo-mechanical modelling. *Tectonophysics*, *746*, 138–154. https://doi.org/10.1016/j.tecto.2017.11.027

Gao, L., Liu, S., Zhang, B., Sun, G., Hu, Y., & Guo, R. (2019). A Ca. 2.8-Ga plume-induced intraoceanic arc system in the eastern North China Craton. *Tectonics*, *38*(5), 1694–1717. https://doi.org/10.1029/2018TC005432

Gerya, T. V. (2010). Dynamical instability produces transform faults at mid-ocean ridges. *Science*, *329*(5995), 1047–1050. https://doi.org/10.1126/science.1191349

Gerya, T. V. (2013). Three-dimensional thermomechanical modeling of oceanic spreading initiation and evolution. *Physics of the Earth and Planetary Interiors*, *214*, 35–52. https://doi.org/10.1016/j.pepi.2012.10.007

Gerya, T. V. (2014). Plume-induced crustal convection: 3D thermomechanical model and implications for the origin of novae and coronae on Venus. *Earth and Planetary Science Letters*, *391*, 183–192. https://doi.org/10.1016/j.epsl.2014.02.005

Gerya, T. V., & Yuen, D. A. (2007). Robust characteristics method for modelling multiphase visco-elasto-plastic thermo-mechanical problems. *Physics of the Earth and Planetary Interiors*, *163*(1–4), 83–105. https://doi.org/10.1016/j.pepi.2007.04.015

Gilmore, M., Treiman, A., Helbert, J., & Smrekar, S. (2017). Venus surface composition constrained by observation and experiment. *Space Science Reviews*, *212*(3–4), 1511–1540. https://doi.org/10.1007/s11214-017-0370-8

Glaze, L. S., Stofan, E. R., Smrekar, S. E., & Baloga, S. M. (2002). Insights into corona formation through statistical analyses: Insights into corona formation. *Journal of Geophysical Research*, *107*(E12), 18–1–18–12. https://doi.org/10.1029/2002JE001904

Gorczyk, W., Mole, D., & Barnes, S. (2018). Plume-lithosphere interaction at craton margins throughout Earth history. *Tectonophysics*, *746*, 678–694. https://doi.org/10.1016/j.tecto.2017.04.002

Griffin, W. (1972). *Formation of eclogites and the coronas in anorthosites, Bergen Arcs, Norway* (Vol. 135, pp. 37–63). Memoir of the Geological Society of America. https://doi.org/10.1130/MEM135-p37

Grimm, R. E. (1994). The deep structure of Venusian plateau highlands. *Icarus*, *112*(1), 89–103. https://doi.org/10.1006/icar.1994.1171

Grindrod, P. M., & Hoogenboom, T. (2006). Venus: The corona conundrum. *Astronomy and Geophysics*, *47*(3), 3.16–3.21. https://doi.org/10.1111/j.1468-4004.2006.47316.x

Gülcher, A. J. P. (2023). Venus coronae topographic (a)symmetry classification (from Gülcher et al., 2023, JGR Planets). *Zenodo*. https://doi.org/10.5281/zenodo.8316805

Gülcher, A. J. P., Beaussier, S. J., & Gerya, T. V. (2019). On the formation of oceanic detachment faults and their influence on intra-oceanic subduction initiation: 3D thermomechanical modeling. *Earth and Planetary Science Letters*, *506*, 195–208. https://doi.org/10.1016/j.epsl.2018.10.042

Gülcher, A. J. P., Gerya, T. V., Montési, L. G. J., & Munch, J. (2020). Corona structures driven by plume–lithosphere interactions and evidence for ongoing plume activity on Venus. *Nature Geoscience*, *13*(8), 547–554. https://doi.org/10.1038/s41561-020-0606-1

Hahn, R. M., & Byrne, P. K. (2023). A morphological and spatial analysis of volcanoes on Venus. *Journal of Geophysical Research: Planets*, *128*(4), e2023JE007753. https://doi.org/10.1029/2023JE007753

Hamilton, V. E., & Stofan, E. R. (1996). The geomorphology and evolution of Hecate chasma, Venus. *Icarus*, *121*(1), 171–194. https://doi.org/10.1006/icar.1996.0077

Harris, L. B., & Bédard, J. H. (2014). Crustal evolution and deformation in a non-plate-tectonic Archaean Earth: Comparisons with Venus. In Y. Dilek & H. Furnes (Eds.), *Evolution of Archean crust and early life* (pp. 215–291). Springer Netherlands. https://doi.org/10.1007/978-94-007-7615-9_9

Hashimoto, G. L., Roos-Serote, M., Sugita, S., Gilmore, M. S., Kamp, L. W., Carlson, R. W., & Baines, K. H. (2008). Felsic highland crust on Venus suggested by Galileo near-infrared mapping spectrometer data. *Journal of Geophysical Research*, *113*(E5), E00B24. https://doi.org/10.1029/2008JE003134

Head, J. W., Crumpler, L. S., Aubele, J. C., Guest, J. E., & Saunders, R. S. (1992). Venus volcanism: Classification of volcanic features and structures, associations, and global distribution from Magellan data. *Journal of Geophysical Research*, *97*(E8), 13153–13197. https://doi.org/10.1029/92JE01273

Herrick, R. R., Bjonnes, E. T., Carter, L. M., Gerya, T., Ghail, R. C., Gillmann, C., et al. (2023). Resurfacing history and volcanic activity of Venus. *Space Science Reviews*, *219*(4), 29. https://doi.org/10.1007/s11214-023-00966-y

Herrick, R. R., & Hensley, S. (2023). Surface changes observed on a Venusian volcano during the Magellan mission. *Science*, *379*(6638), 1205–1208. https://doi.org/10.1126/science.abm7735

Herrick, R. R., & Rumpf, M. E. (2011). Postimpact modification by volcanic or tectonic processes as the rule, not the exception, for Venusian craters. *Journal of Geophysical Research*, *116*(E2), E02004. https://doi.org/10.1029/2010JE003722

Ito, K., & Kennedy, G. C. (1971). An experimental study of the basalt-garnet granulite-eclogite transition. In J. G. Heacock (Ed.), *The structure and physical properties of the Earth's crust* (Vol. 14, pp. 303–314). American Geophysical Union. https://doi.org/10.1029/GM014p0303

Ivanov, M. A., & Head, J. W. (1996). Tessera terrain on Venus: A survey of the global distribution, characteristics, and relation to surrounding units from Magellan data. *Journal of Geophysical Research*, *101*(E6), 14861–14908. https://doi.org/10.1029/96JE01245

Ivanov, M. A., & Head, J. W. (2011). Global geological map of Venus. *Planetary and Space Science*, *59*(13), 1559–1600. https://doi.org/10.1016/j.pss.2011.07.008

James, P. B., Zuber, M. T., & Phillips, R. J. (2013). Crustal thickness and support of topography on Venus. *Journal of Geophysical Research: Planets*, *118*(4), 859–875. https://doi.org/10.1029/2012JE004237

Jellinek, A. M. (2002). The influence of interior mantle temperature on the structure of plumes: Heads for Venus, Tails for the Earth. *Geophysical Research Letters*, *29*(11), 1532. https://doi.org/10.1029/2001GL014624

Jennings, S., Heinson, G., Hasterok, D., & Kay, B. (2023). Magnetotelluric support for edge-driven convection and shear-driven upwelling in the Newer Volcanics Province. *Scientific Reports*, *13*(1), 5543. https://doi.org/10.1038/s41598-023-32403-z

Jiménez-Díaz, A., Ruiz, J., Kirby, J. F., Romeo, I., Tejero, R., & Capote, R. (2015). Lithospheric structure of Venus from gravity and topography. *Icarus*, *260*, 215–231. https://doi.org/10.1016/j.icarus.2015.07.020

Johnson, C. L., & Richards, M. A. (2003). A conceptual model for the relationship between coronae and large-scale mantle dynamics on Venus. *Journal of Geophysical Research*, *108*(E6), 5058. https://doi.org/10.1029/2002JE001962

Kaislaniemi, L., & Van Hunen, J. (2014). Dynamics of lithospheric thinning and mantle melting by edge-driven convection: Application to Moroccan Atlas Mountains. *Geochemistry, Geophysics, Geosystems*, *15*(8), 3175–3189. https://doi.org/10.1002/2014GC005414

Katz, R. F., Spiegelman, M., & Langmuir, C. H. (2003). A new parameterization of hydrous mantle melting. *Geochemistry, Geophysics, Geosystems*, *4*(9), 1073. https://doi.org/10.1029/2002GC000433

King, S. D., & Anderson, D. L. (1998). Edge-driven convection. *Earth and Planetary Science Letters*, *160*(3–4), 289–296. https://doi.org/10.1016/S0012-821X(98)00089-2

Koptev, A., Calais, E., Burov, E. B., Leroy, S., & Gerya, T. V. (2015). Dual continental rift systems generated by plume-lithosphere interaction. *Nature Geoscience*, *8*(5), 388–392. https://doi.org/10.1038/ngeo2401

Krassilnikov, A. S., & Head, J. W. (2003). Novae on Venus: Geology, classification, and evolution. *Journal of Geophysical Research*, *108*(E9), 5108. https://doi.org/10.1029/2002JE001983

Kufner, S.-K., Kakar, N., Bezada, M., Bloch, W., Metzger, S., Yuan, X., et al. (2021). The Hindu Kush slab break-off as revealed by deep structure and crustal deformation. *Nature Communications*, *12*(1), 1685. https://doi.org/10.1038/s41467-021-21760-w

Lourenço, D. L., Rozel, A. B., Ballmer, M. D., & Tackley, P. J. (2020). Plutonic-squishy lid: A new global tectonic regime generated by intrusive magmatism on Earth-like planets. *Geochemistry, Geophysics, Geosystems*, *21*(4), e2019GC008756. https://doi.org/10.1029/2019GC008756

Maia, J. S., & Wieczorek, M. A. (2022). Lithospheric structure of Venusian crustal plateaus. *Journal of Geophysical Research: Planets*, *127*(2), e2021JE007004. https://doi.org/10.1029/2021JE007004

McKenzie, D. P., Ford, P. G., Johnson, C. L., Parsons, B., Sandwell, D. T., Saunders, R. S., & Solomon, S. C. (1992). Features on Venus generated by plate boundary processes. *Journal of Geophysical Research*, *97*(E8), 13533–13544. https://doi.org/10.1029/92JE01350

Nimmo, F., & Mackwell, S. (2023). Viscous relaxation as a probe of heat flux and crustal plateau composition on Venus. *Proceedings of the National Academy of Sciences*, *120*(3), e2216311120. https://doi.org/10.1073/pnas.2216311120

O'Rourke, J. G., & Smrekar, S. E. (2018). Signatures of lithospheric flexure and elevated heat flow in stereo topography at coronae on Venus: Lithospheric flexure at coronae on Venus. *Journal of Geophysical Research: Planets*, *123*(2), 369–389. https://doi.org/10.1002/2017JE005358

O'Rourke, J. G., Wilson, C. F., Borrelli, M. E., Byrne, P. K., Dumoulin, C., Ghail, R., et al. (2023). Venus, the planet: Introduction to the evolution of Earth's Sister planet. *Space Science Reviews*, *219*(1), 10. https://doi.org/10.1007/s11214-023-00956-0

Perchuk, A. L., Zakharov, V. S., Gerya, T. V., & Griffin, W. L. (2023). Flat subduction in the Early Earth: The key role of discrete eclogitization kinetics. *Gondwana Research*, *119*, 186–203. https://doi.org/10.1016/j.gr.2023.03.015

Pettengill, G. H., Ford, P. G., Johnson, W. T. K., Raney, R. K., & Soderblom, L. A. (1991). Magellan: Radar performance and data products. *Science*, *252*(5003), 260–265. https://doi.org/10.1126/science.252.5003.260

Phillips, R. J., & Malin, M. C. (1983). The interior of Venus and tectonic implications. In D. Hunten, L. Colin, V. Moroz, & T. Donahue (Eds.), *Venus* (pp. 159–214). University of Arizona Press.

Piskorz, D., Elkins-Tanton, L. T., & Smrekar, S. E. (2014). Coronae formation on Venus via extension and lithospheric instability. *Journal of Geophysical Research: Planets*, *119*(12), 2568–2582. https://doi.org/10.1002/2014JE004636

Price, M. H., Watson, G., Suppe, J., & Brankman, C. (1996). Dating volcanism and rifting on Venus using impact crater densities. *Journal of Geophysical Research*, *101*(E2), 4657–4671. https://doi.org/10.1029/95JE03017

Ranalli, G. (1995). *Rheology of the Earth*. Springer.

Robin, C., Jellinek, A., Thayalan, V., & Lenardic, A. (2007). Transient mantle convection on Venus: The paradoxical coexistence of highlands and coronae in the BAT region. *Earth and Planetary Science Letters*, *256*(1–2), 100–119. https://doi.org/10.1016/j.epsl.2007.01.016

Rodriguez, M., Arnould, M., Coltice, N., & Soret, M. (2021). Long-term evolution of a plume-induced subduction in the Neotethys realm. *Earth and Planetary Science Letters*, *561*, 116798. https://doi.org/10.1016/j.epsl.2021.116798

Rolf, T., Weller, M., Gülcher, A., Byrne, P., O'Rourke, J. G., Herrick, R., et al. (2022). Dynamics and evolution of Venus' mantle through time. *Space Science Reviews*, *218*(8), 70. https://doi.org/10.1007/s11214-022-00937-9

Russell, M. B., & Johnson, C. L. (2021). Evidence for a locally thinned lithosphere associated with recent volcanism at Aramaiti Corona, Venus. *Journal of Geophysical Research: Planets*, *126*(8), e2020JE006783. https://doi.org/10.1029/2020JE006783

Sandwell, D. T. (2015). Global topography and SAR files from Magellan Venus data. Retrieved from https://topex.ucsd.edu/pub/sandwell/google/venus/

Sandwell, D. T., Johnson, C. L., Bilotti, F., & Suppe, J. (1997). Driving forces for limited tectonics on Venus. *Icarus*, *129*(1), 232–244. https://doi.org/10.1006/icar.1997.5721

Sandwell, D. T., & Schubert, G. (1992). Evidence for retrograde lithospheric subduction on Venus. *Science*, *257*(5071), 766–770. https://doi.org/10.1126/science.257.5071.766

Saunders, R. S., Pettengill, G. H., Arvidson, R. E., Sjogren, W. L., Johnson, W. T. K., & Pieri, L. (1990). The Magellan Venus radar mapping mission. *Journal of Geophysical Research*, *95*(B6), 8339–8355. https://doi.org/10.1029/JB095iB06p08339

Schmeling, H., Babeyko, A. Y., Enns, A., Faccenna, C., Funiciello, F., Gerya, T. V., et al. (2008). A benchmark comparison of spontaneous subduction models-Towards a free surface. *Physics of the Earth and Planetary Interiors*, *171*(1–4), 198–223. https://doi.org/10.1016/j.pepi.2008.06.028

Simons, M., Solomon, S. C., & Hager, B. H. (1997). Localization of gravity and topography: Constraints on the tectonics and mantle dynamics of Venus. *Geophysical Journal International*, *131*(1), 24–44. https://doi.org/10.1111/j.1365-246X.1997.tb00593.x

Smrekar, S. E., Hensley, S., Nybakken, R., Wallace, M. S., Perkovic-Martin, D., You, T.-H., et al. (2022). VERITAS (Venus emissivity, radio science, InSAR, topography, and spectroscopy): A discovery mission. In *In 2022 IEEE aerospace conference (AERO)* (pp. 1–20). https://doi.org/10.1109/AERO53065.2022.9843269

Smrekar, S. E., Ostberg, C., & O'Rourke, J. G. (2023). Earth-like lithospheric thickness and heat flow on Venus consistent with active rifting. *Nature Geoscience*, *16*(1), 13–18. https://doi.org/10.1038/s41561-022-01068-0

Smrekar, S. E., & Phillips, R. J. (1991). Venusian highlands: Geoid to topography ratios and their implications. *Earth and Planetary Science Letters*, *107*(3–4), 582–597. https://doi.org/10.1016/0012-821X(91)90103-O

Smrekar, S. E., & Stofan, E. R. (1997). Corona formation and heat loss on Venus by coupled upwelling and delamination. *Science*, *277*(5330), 1289–1294. https://doi.org/10.1126/science.277.5330.1289

Smrekar, S. E., & Stofan, E. R. (1999). Origin of corona-dominated topographic rises on Venus. *Icarus*, *139*(1), 100–115. https://doi.org/10.1006/icar.1999.6090

Smrekar, S. E., Stofan, E. R., Mueller, N., Treiman, A., Elkins-Tanton, L. T., Helbert, J., et al. (2010). Recent hotspot volcanism on Venus from VIRTIS emissivity data. *Science*, *328*(5978), 605–608. https://doi.org/10.1126/science.1186785

Stern, R. J., & Dumitru, T. A. (2019). Eocene initiation of the Cascadia subduction zone: A second example of plume-induced subduction initiation? *Geosphere*, *15*(3), 659–681. https://doi.org/10.1130/GES02050.1

Stofan, E. R., Sharpton, V. L., Schubert, G., Baer, G., Bindschadler, L., Janes, D. M., & Squyres, W. (1992). Global distribution and characteristics of coronae and related features on Venus: Implications for origin and relation to mantle processes. *Journal of Geophysical Research*, *97*(92), 347–378. https://doi.org/10.1029/92je01314

Stofan, E. R., Smrekar, S. E., Bindschadler, D. L., & Senske, D. A. (1995). Large topographic rises on Venus: Implications for mantle upwelling. *Journal of Geophysical Research*, *100*(E11), 23317–23327. https://doi.org/10.1029/95JE01834

Stofan, E. R., Smrekar, S. E., Tapper, S. W., Guest, J. E., & Grindrod, P. M. (2001). Preliminary analysis of an expanded corona database for Venus. *Geophysical Research Letters*, *28*(22), 4267–4270. https://doi.org/10.1029/2001GL013307

Strom, R. G., Schaber, G. G., & Dawson, D. D. (1994). The global resurfacing of Venus. *Journal of Geophysical Research*, *99*(E5), 10899–10926. https://doi.org/10.1029/94JE00388

Surkov, Y. A., Barsukov, V. L., Moskalyeva, L. P., Kharyukova, V. P., & Kemurdzhian, A. L. (1984). New data on the composition, structure, and properties of Venus rock obtained by Venera 13 and Venera 14. *Journal of Geophysical Research*, *89*(S02), B393. https://doi.org/10.1029/JB089iS02p0B393

Turcotte, D. L. (1993). An episodic hypothesis for Venusian tectonics. *Journal of Geophysical Research*, *98*(E9), 17061–17068. https://doi.org/10.1029/93JE01775

Turcotte, D. L., & Schubert, G. (2002). *Geodynamics*. Cambridge University Press.

Ueda, K., Gerya, T. V., & Sobolev, S. V. (2008). Subduction initiation by thermal-chemical plumes: Numerical studies. *Physics of the Earth and Planetary Interiors*, *171*(1–4), 296–312. https://doi.org/10.1016/j.pepi.2008.06.032

U.S. Geological Survey. (2023). Gazetteer of planetary nomenclature. Retrieved from https://planetarynames.wr.usgs.gov/Page/VENUS/target

Van Hunen, J., Van Den Berg, A. P., & Vlaar, N. J. (2004). Various mechanisms to induce present-day shallow flat subduction and implications for the younger Earth: A numerical parameter study. *Physics of the Earth and Planetary Interiors*, *146*(1–2), 179–194. https://doi.org/10.1016/j.pepi.2003.07.027

Van Wijk, J., Baldridge, W., Van Hunen, J., Goes, S., Aster, R., Coblentz, D., et al. (2010). Small-scale convection at the edge of the Colorado Plateau: Implications for topography, magmatism, and evolution of Proterozoic lithosphere. *Geology*, *38*(7), 611–614. https://doi.org/10.1130/G31031.1

Vogt, P. R. (1991). Bermuda and Appalachian-Labrador rises: Common non-hotspot processes? *Geology*, *19*(1), 41. https://doi.org/10.1130/0091-7613(1991)019〈0041:BAALRC〉2.3.CO;2

Wessel, P., & Luis, J. F. (2017). The GMT/MATLAB toolbox. *Geochemistry, Geophysics, Geosystems*, *18*(2), 811–823. https://doi.org/10.1002/2016GC006723.Received

Wieczorek, M. A. (2015). Gravity and topography of the terrestrial planets. In *Treatise on geophysics* (2nd ed., Vol. 10, pp. 153–193). https://doi.org/10.1016/B978-0-444-53802-4.00169-X

Zhan, Z., & Kanamori, H. (2016). Recurring large deep earthquakes in Hindu Kush driven by a sinking slab: Recurring Hindu Kush Earthquakes. *Geophysical Research Letters*, *43*(14), 7433–7441. https://doi.org/10.1002/2016GL069603

Zhang, R. Y., & Liou, J. G. (1997). Partial transformation of gabbro to coesite-bearing eclogite from Yangkou, the Sulu terrane, eastern China: Partial transformation of gabbro to eclogite. *Journal of Metamorphic Geology*, *15*(2), 183–202. https://doi.org/10.1111/j.1525-1314.1997.00012.x